

# Enhancing Monocular Height Estimation via Sparse LiDAR-Guided Correction

Jian Song<sup>a,b</sup>, Hongruixuan Chen<sup>a,b</sup> and Naoto Yokoya<sup>a,b,\*</sup>

<sup>a</sup>Graduate School of Frontier Sciences, The University of Tokyo, Chiba, 277-8561, Japan

<sup>b</sup>RIKEN Center for Advanced Intelligence Project (AIP), RIKEN, Tokyo, 103-0027, Japan

## ARTICLE INFO

### Keywords:

Monocular Height Estimation  
Network Interpretability  
ICESat-2 Data  
Sparse LiDAR-based Calibration  
Machine Learning

## ABSTRACT

Monocular height estimation (MHE) from very-high-resolution (VHR) remote sensing imagery via deep learning is notoriously challenging due to the lack of sufficient structural information. Conventional digital elevation models (DEMs), typically derived from airborne LiDAR or multi-view stereo, remain costly and geographically limited. Recently, models trained on synthetic data and refined through domain adaptation have shown remarkable performance in MHE, yet it remains unclear how these models make predictions or how reliable they truly are. In this paper, we investigate a state-of-the-art MHE model trained purely on synthetic data to explore *where* the model looks when making height predictions. Through systematic analyses, we find that the model relies heavily on shadow cues, a factor that can lead to overestimation or underestimation of heights when shadows deviate from expected norms. Furthermore, the inherent difficulty of evaluating regression tasks with the human eye underscores additional limitations of purely synthetic training. To address these issues, we propose a novel correction pipeline that integrates sparse, imperfect global LiDAR measurements (*ICESat-2*) with deep-learning outputs to improve local accuracy and achieve spatially consistent corrections. Our method comprises two stages: pre-processing raw *ICESat-2* data, followed by a random forest-based approach to densely refine height estimates. Experiments in three representative urban regions—Saint-Omer, Tokyo, and São Paulo—reveal substantial error reductions, with mean absolute error (MAE) decreased by 22.8%, 6.9%, and 4.9%, respectively. These findings highlight the critical role of shadow awareness in synthetic data-driven models and demonstrate how fusing imperfect real-world LiDAR data can bolster the robustness of MHE, paving the way for more reliable and scalable 3D mapping solutions.

## 1. Introduction

Very-high-resolution (VHR) sensors enable increasingly detailed observations of the Earth, providing diverse data modalities that enrich our understanding of surface conditions. For instance, the WorldView<sup>1</sup> satellite series can now offer sub-meter ground-sampling distance (GSD) optical imagery, as well as multispectral/hyperspectral data<sup>2</sup> (capturing multiple spectral bands for enhanced material and vegetation analysis) and synthetic aperture radar (SAR) data (capable of all-weather, day-and-night imaging) (Chen et al., 2025; Xia et al., 2025). Among these modalities, VHR digital elevation models (DEMs), which capture the elevation of terrain and above-ground objects, play a pivotal role in urban planning, environmental monitoring, disaster management, 3D mapping, and digital twin applications (Li et al., 2023, 2019, 2021, 2024, 2020b; Mao et al., 2023).

Although moderate- to low-resolution DEMs (5 m or coarser), such as SRTM (NASA, 2002), ASTER (METI, 2009), ALOS PALSAR (JAXA, 2008), and TanDEM (DLR, 2010), are freely available on a global scale, obtaining sub-meter DEMs traditionally relies on methods like airborne LiDAR (Hermosilla et al., 2011; Li et al., 2020a; Sohn and Dowman, 2004), stereo vision matching (Ameri et al., 2002;

Han et al., 2020; Liu et al., 2023; Mahphood et al., 2019; Yu et al., 2021a; Zhang et al., 2003), or InSAR (Wang et al., 2024; Yu et al., 2015)—techniques that are both expensive and time-consuming. For example, based on AW3D<sup>3</sup>'s<sup>3</sup> per-square-kilometer pricing, generating a 0.5 m GSD DEM of Japan through stereo matching could cost up to 20 million dollars. Similarly, the French HD LiDAR project<sup>4</sup> estimates that acquiring nationwide LiDAR coverage of France would require an investment of nearly 60 million euros and take about five years. Such high costs and limited scalability have hindered the widespread global adoption of high-resolution DEM applications.

The recent rise of deep learning offers a promising alternative (Gao et al., 2023c; Ghamisi and Yokoya, 2018a; Gordon et al., 2020; Kunwar, 2019a; Li et al., 2023, 2019, 2021, 2024, 2020b; Mao et al., 2023; Srivastava et al., 2017; Zheng et al., 2019). Researchers have explored using machine learning, particularly *monocular height estimation* (MHE), to infer elevations from a single VHR remote sensing optical image, greatly reducing costs and allowing for broad scalability. Yet, like traditional approaches, deep learning models require extensive labeled data, which remains difficult to obtain at sub-meter resolution on a global scale. Moreover, deep learning is famously data-hungry: greater quantities of more diverse training data typically yield better model performance (Krizhevsky et al.,

Manuscript submitted on April 14, 2025.

\*Corresponding author

ORCID(s): 0009-0001-5577-8595 (J. Song)

<sup>1</sup><https://earth.esa.int/eogateway/missions/worldview-3>

<sup>2</sup>[https://www.ehu.eus/ccwintco/index.php?title=Hyperspectral\\_](https://www.ehu.eus/ccwintco/index.php?title=Hyperspectral_Remote_Sensing_Scenes)

[Remote\\_Sensing\\_Scenes](https://www.ehu.eus/ccwintco/index.php?title=Hyperspectral_Remote_Sensing_Scenes)

<sup>3</sup><https://net.jmc.or.jp/mapdata/3d/aw3d/enhanced.html>

<sup>4</sup><https://diffusion-lidarhd.ign.fr/mnx/>

2012). However, remote sensing data often exhibit geographic biases—abundant in developed regions but scarce elsewhere—leading to inductive bias in models trained predominantly on real-world data (Schmitt et al., 2023), thereby limiting the overall applicability of MHE to different regions.

In response, synthetic datasets (Bourdis et al., 2011; Kong et al., 2020; Reyes et al., 2022, 2023; Shermeyer et al., 2021; Song et al., 2024a,b; Xiong et al., 2023; Xu et al., 2022; Zou et al., 2020) have emerged as a potential solution. For example, SynRS3D (Song et al., 2024a) comprises 69,667 image pairs with semantic segmentation labels and ground-truth elevations, and models trained on it via unsupervised domain adaptation (UDA) have outperformed real-data-trained counterparts on multiple benchmark datasets, demonstrating strong generalization capability. Nevertheless, the internal workings of deep learning models remain largely opaque—particularly in MHE, a complex task in which human observers typically rely on shadow cues to infer object heights. It is not yet clear whether neural networks adopt a similar mechanism. Few studies have systematically investigated how MHE networks trained on synthetic data arrive at their predictions, despite the importance of this knowledge for understanding model behavior and guiding further improvements.

To address this gap, we employed a synthetic environment to simulate different illumination and texture conditions for the same scene, examining the underlying prediction mechanisms of the state-of-the-art MHE model RS3DAda (Song et al., 2024a). Our findings suggest that the model heavily depend on shadow cues: when shadow lengths fall outside expected ranges, the network’s predictions can be significantly under- or overestimated, ultimately undermining reliability. Moreover, in contrast to tasks such as semantic segmentation or land-cover mapping—whose large-scale outputs can be checked via expert interpretation—MHE results cannot be easily validated through human inspection alone, as humans cannot directly perceive exact heights from a single image.

On the other hand, while acquiring dense sub-meter DEMs globally remains prohibitively expensive, some imperfect yet globally available elevation data do exist. Instruments like NASA’s GEDI<sup>5</sup> and ICESat-2<sup>6</sup> provide physically measured heights along sparse ground tracks; ICESat-2, in particular, covers the entire planet, features a high revisit rate, and offers fine along-track resolution. Despite its sparse sampling, ICESat-2 data can crucially inform post-processing steps to correct synthetic-data-driven MHE, helping alleviate the bias introduced by an overreliance on shadow cues.

Accordingly, we propose a post-processing correction workflow that leverages ICESat-2 data to refine dense height predictions produced by deep learning models. This workflow comprises two main steps: preprocessing raw ICESat-2 data and then training a random forest model to correct

the dense predictions on a global scale. We evaluate our approach in three geographically distinct urban areas—Saint-Omer, Tokyo, and São Paulo—and demonstrate that it effectively and efficiently reduces errors in monocular height estimation.

Our key contributions are as follows:

1. Through controlled experiments in a synthetic environment with varying illumination and texture settings, we systematically analyze the prediction mechanisms of the MHE network trained on synthetic data, identifying shadow-dependent biases and potential reliability issues.
2. Motivated by this analysis, we introduce an ICESat-2-based post-processing workflow for MHE model’s prediction and validate its effectiveness across three globally distinct regions.

## 2. Related Work

This study encompasses several domains, including MHE model visualization and interpretability, ICESat-2 data preprocessing techniques, as well as random-forest-based post-processing as calibration step for dense height predictions. Our aim is to achieve accurate and reliable high-resolution elevation mapping without resorting to expensive and dense real-world data. In this section, we systematically review the relevant literature across the following areas.

### 2.1. Monocular Height Estimation

Compared with traditional methods of acquiring elevation data—such as airborne LiDAR (Hermosilla et al., 2011; Li et al., 2020a; Sohn and Dowman, 2004), stereo-vision matching (Ameri et al., 2002; Han et al., 2020; Liu et al., 2023; Mahphood et al., 2019; Yu et al., 2021a; Zhang et al., 2003), or InSAR (Wang et al., 2024; Yu et al., 2015)—deep-learning-based monocular height estimation (MHE) is more cost-effective, efficient, and scalable. Similar to depth estimation in computer vision, remote sensing height estimation comprises multi-view (Favalli et al., 2012; Gao et al., 2023a; Hu et al., 2021; Leotta et al., 2019; Rupnik et al., 2018; Yu et al., 2021b) and single-view approaches. While multi-view methods require multiple high-resolution images, single-view methods need only one. Although more challenging, single-view approaches significantly reduce data costs.

Given a high-resolution optical image, the goal is to produce a per-pixel above-ground height map, a typical regression task. Earlier works, such as (Srivastava et al., 2017), proposed multi-task deep learning frameworks to jointly predict height and semantic labels. Others employed residual CNNs for height estimation and validated their effectiveness in instance segmentation (Mou and Zhu, 2018). Conditional generative adversarial networks (cGANs) have also been applied, treating single-view height estimation as an image translation problem (Ghamisi and Yokoya, 2018b). Additional studies leverage semantic priors to enhance height predictions (Kunwar, 2019b), while some focus on large-scale cross-dataset transfer learning (Xiong et al., 2023). Some

<sup>5</sup><https://gedi.umd.edu/>

<sup>6</sup><https://icesat-2.gsfc.nasa.gov/>

methods (Chen et al., 2023) treat MHE purely as a classification task by discretizing continuous height values into predefined bins, rather than formulating it as a regression problem. Recent methods incorporate Transformer (Vaswani, 2017) encoders and decoders to improve the transferability of representations. RS3DAda (Song et al., 2024a), in particular, integrates advanced encoders like DINOv2 (Oquab et al., 2023) with decoders such as DPT (Ranftl et al., 2021) to achieve state-of-the-art performance in MHE. Our proposed post-processing pipeline builds upon the RS3DAda’s output, further refining its predictions.

## 2.2. Network Interpretability

Network interpretability is critical for uncovering how deep neural networks function internally and for determining which parts of the input exert the strongest influence on their decisions. This insight can drive valuable improvements in network architecture. Recently, a growing number of researchers have turned their attention to saliency- and attribution-based methods for explainable deep networks (Garcke and Roscher, 2023; Obadic et al., 2022; Roscher et al., 2020). In addition, popular visualization approaches—such as feature-map visualization, t-SNE (Van der Maaten and Hinton, 2008), UMAP (McInnes et al., 2018), and Grad-CAM (Selvaraju et al., 2017)—offer varying degrees of clarity on the spatial and semantic cues the network attends to during inference.

In conventional computer vision for depth estimation, some researchers have investigated interpretability more explicitly. For instance, one study (Hu et al., 2019) formulated an optimization approach to identify the minimal set of pixels that most strongly influence the CNN’s depth predictions, finding that a relatively small region can yield near-complete reconstruction quality. Another work (Dijk and Croon, 2019) focused on how different camera pitch and roll angles affect the use of depth cues, noting significant performance drops when camera angles deviate from training conditions. Further, certain methods (You et al., 2021) examined hidden units selective to specific depth ranges and proposed training strategies that boost unit-wise selectivity—and thus interpretability—without compromising accuracy.

In remote sensing, (Xiong et al., 2024) conducted a preliminary investigation of MHE networks, revealing correlations between predicted height and semantic information. However, they did not probe which image regions or factors primarily drive the network’s inferences. Here, we perform a novel, systematic analysis in a controlled synthetic environment where varying illumination and textures for the same scene allow us to pinpoint how and where the network focuses in making height predictions, representing the first in-depth interpretability study for monocular remote sensing height estimation.

## 2.3. ICESat-2 Data

Launched by NASA at 2018, the Ice, Cloud, and Land Elevation Satellite-2 (ICESat-2) uses the Advanced Topographic Laser Altimeter System (ATLAS) system to deliver high-precision surface elevation measurements at global

scale. Compared with other spaceborne LiDAR systems (e.g., GEDI), ICESat-2 offers broader coverage, shorter revisit intervals, and higher along-track sampling density, making it well-suited for worldwide elevation applications.

While many studies leverage ICESat-2 data to estimate specific objects’ heights (e.g., buildings or forest canopies) (Dubayah et al., 2022; Huang et al., 2024; Lao et al., 2021; Qi and Dubayah, 2016; Schneider et al., 2020; Shendryk, 2022; Wu et al., 2023; Zhao et al., 2023), they typically focus on a limited area or require auxiliary datasets, thus limiting large-scale deployment. Moreover, ICESat-2’s sampling remains relatively sparse, making it challenging to capture the complex vertical structures present in urban environments. Recent research has sought to fuse ICESat-2 with other remote sensing modalities (Li et al., 2020a; Tang et al., 2025; Zhang et al., 2019), but such fusion often relies on existing low- or medium-resolution datasets that may lack the detail necessary for sub-meter urban mapping.

To overcome these limitations, we propose a post-processing correction pipeline that integrates the dense height predictions generated by the state-of-the-art MHE model RS3DAda (Song et al., 2024a) with sparse ICESat-2 measurements via a random forest model (Breiman, 2001). Our method is applicable worldwide, requiring only a geo-referenced VHR optical image, regional ICESat-2 data along track, and the MHE model’s output to produce a high-fidelity, high-resolution normalized Digital Elevation Model (nDSM). We detail this workflow and validate its effectiveness in the following sections.

## 3. Where is MHE Model Looking?

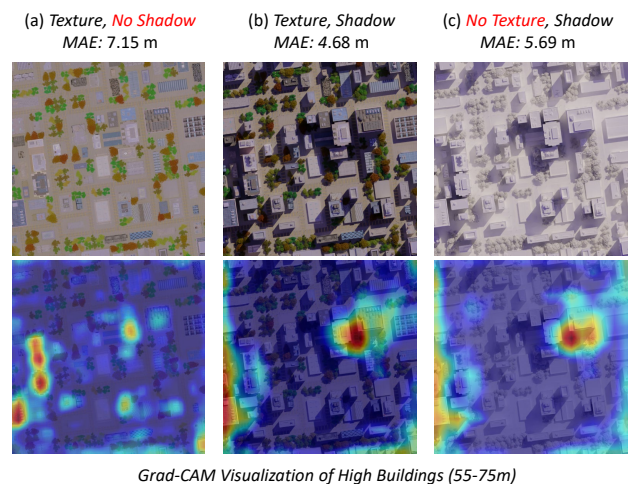


**Figure 1:** Visualization of three different lighting/texturing conditions (top row) and their corresponding Grad-CAM attention maps for tall buildings (bottom row). From left to right: (a) texture without shadows, (b) texture with shadows, and (c) shadows with texture removed. Mean Absolute Error (MAE) values quantify estimation accuracy.

Estimating object heights from a single remote sensing image (MHE) is notably challenging. While humans can

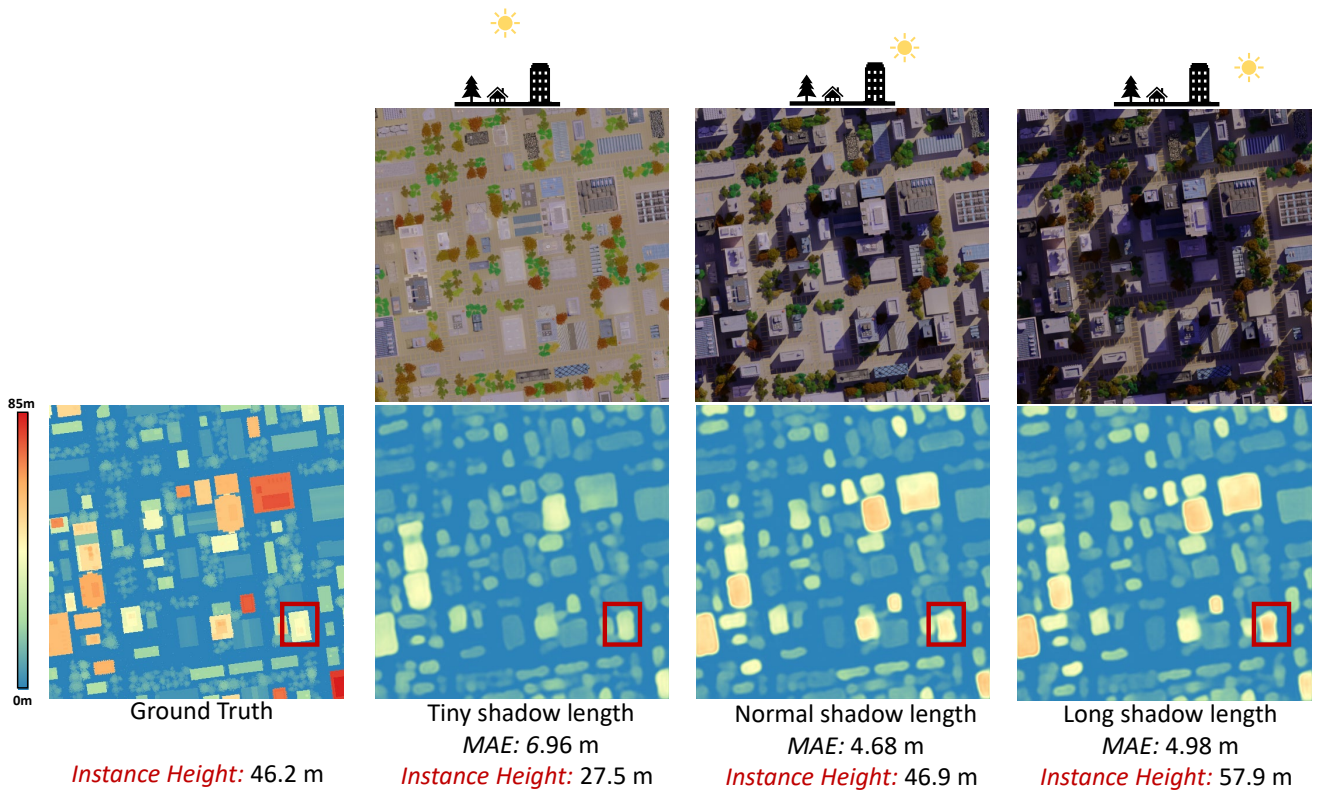


**Figure 2:** Investigating the effect of different shadow lengths on height estimation. From left to right: ground-truth height map, tiny shadow length, normal shadow length, and long shadow length. The corresponding MAE values and example building-height predictions (red boxes) highlight how extreme shadow conditions degrade estimation accuracy.

easily recognize objects and their categories from appearance, accurately inferring object heights from a single view is far more difficult. Surprisingly, deep learning models have demonstrated strong performance in MHE. This raises two key questions: which cues are these models using, and *where* do they “look” in an image to estimate height?

To investigate these questions, a series of visualization experiments was conducted on a state-of-the-art method for MHE proposed in (Song et al., 2024a), hereafter referred to as the “MHE model.” The results reveal that *shadows* serve as critical cues for height prediction. The following subsections detail how controlled synthetic environments help isolate and evaluate the role of shadows in the model’s decision-making process.

### 3.1. Shadows as Key Cues

A significant advantage of using a procedural city-synthesis system (Song et al., 2024a,b) is that it can generate identical scenes under varying illumination settings, an approach that would be prohibitively difficult with real satellite imagery. Figure 1 (top row) illustrates three versions of the same synthetic scene:

1. *No shadows, with texture,*
2. *Normal-length shadows with texture,*
3. *Normal-length shadows but with texture removed.*

All three configurations share the same ground-truth height map. The MHE model is applied to each image, and the per-pixel height predictions are evaluated with Mean Absolute Error (MAE). Gradient-weighted Class Activation Mapping (Grad-CAM) (Selvaraju et al., 2017) further highlights which regions the model attends to when predicting the heights of taller buildings (55–75 m).

In the absence of shadows (condition 1), the model yields a relatively large MAE of 7.15 m and predominantly focuses on building rooftops. When both texture and shadows are present (condition 2), the model achieves its best performance (MAE of 4.68 m), and Grad-CAM maps clearly concentrate on shadowed areas. This indicates that shadows provide essential cues that improve accuracy. Even if texture is removed while retaining shadows (condition 3), the MAE remains comparatively low (5.69 m), suggesting that shadows alone enable reasonably accurate height estimates. These results imply that *shadow features matter more than texture cues* for this particular model, aligning with intuitive human perception wherein shadows also serve as essential depth cues.

### 3.2. Impact of Varying Shadow Lengths

To further assess the effect of shadows, three illumination conditions were synthesized by adjusting the sun’s position:

1. *Nearly no shadows,*

2. Moderate/normal shadow length,
3. Excessively long shadows.

All other scene parameters remained fixed, and the ground-truth height map stayed the same. As shown in Figure 2, very short shadows produce the highest MAE (6.96 m), whereas moderate shadows lead to the lowest MAE (4.68 m), thereby yielding the most accurate predictions. Long shadows result in a slight overestimation of building heights (MAE of 4.98 m), causing the overall predicted height distribution to shift upward. These findings suggest that while the monocular model benefits greatly from shadow information, extreme shadow conditions (either too short or too long) can degrade performance.

In summary, these controlled experiments demonstrate a strong reliance on shadow cues for single-image height estimation in high-resolution remote sensing imagery. When illumination deviates from the “normal” range, the model tends to either under- or overestimate building heights. This indicates a need for complementary data sources or corrective methods, especially under extreme lighting conditions. The next section explores how integrating sparse real-world LiDAR measurements can mitigate such biases and improve the robustness of the estimated height maps.

## 4. Height Estimates Calibration with ICESat-2

### 4.1. Motivation and Overview

Building on the mechanism analysis in Section 3, the MHE model can perform well on large-scale optical imagery but often rely heavily on shadow cues. While this reliance can be effective under normal illumination, it introduces uncertainty under extreme or atypical lighting conditions. Moreover, even if an MHE model achieves promising validation metrics, the *continuous* nature of height outputs poses an inherent challenge for large-scale remote sensing applications.

Unlike *classification* tasks (where discrete labels such as “tree” or “water” can be visually cross-checked), height estimation produces numerical values that people cannot reliably verify by sight alone. Figure 3 illustrates how individuals may easily recognize an object as a tree yet be unable to judge whether it stands 3 m, 7 m, or 16 m tall (Brenner and van Damme, 1999; Kolarik et al., 2016). Consequently, while classification maps can often be validated through *visual inspection*, continuous variables like height *require* reference data to confirm or adjust the model’s predictions (Bingham and Pagano, 1998).

From a remote sensing perspective, these perceptual limitations underscore the need for an external data source to *anchor* or *correct* MHE estimates. Sparse but highly accurate LiDAR measurements, such as those from GEDI or ICESat-2, are particularly appealing for this purpose. Even though they only provide a limited number of high-precision samples, such measurements can highlight and correct systematic biases in MHE models (e.g., shadow-induced misestimations). This section therefore presents the

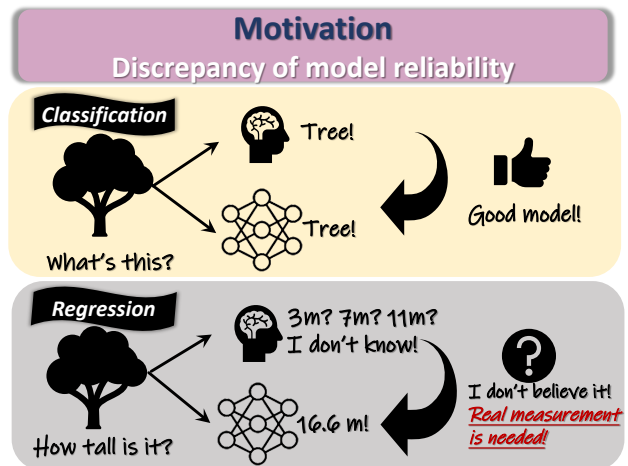


**Figure 3:** Motivation: discrepancy in model reliability for classification vs. regression. Humans can easily check if an object is a “tree” (top), but cannot intuitively decide if that tree is 3 m, 7 m, or 16.6 m tall (bottom). External measurements are crucial to validate or adjust continuous outputs.

case for leveraging ICESat-2 data to refine large-scale height predictions and reduce the impact of model uncertainty.

### 4.2. ICESat-2 Data Specifications

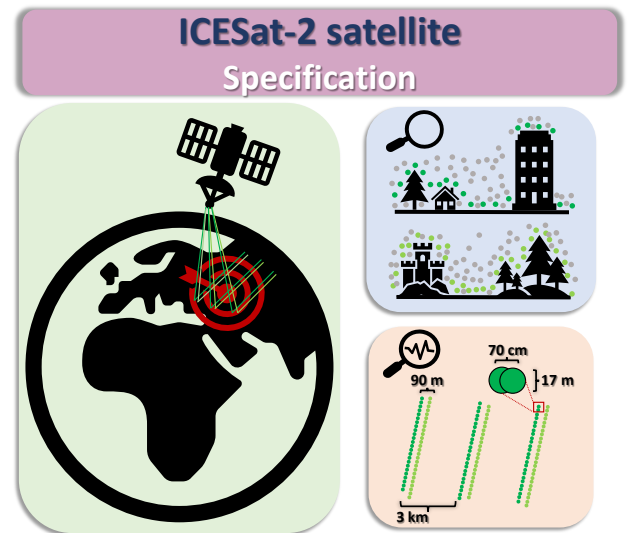


**Figure 4:** Highlights of the ICESat-2 mission, illustrating near-global coverage, tightly spaced along-track photons, and beam configurations designed to distinguish ground from canopy returns.

Before describing how ICESat-2 measurements are integrated into a calibration pipeline (Section 5), it is essential to review key mission parameters that make ICESat-2 especially suitable for validating and correcting synthetic-data-driven MHE models.

**Table 1**  
Comparison of key parameters for GEDI and ICESat-2.

Parameter	GEDI	ICESat-2
Platform	ISS-mounted instrument	Dedicated Earth-observing satellite
Coverage	$\pm 51^\circ$ latitude	$\pm 88^\circ$ latitude
Orbit Altitude	$\sim 400$ km (ISS orbit)	$\sim 500$ km
Laser Beams	3 beams (2 cover, 1 reference)	6 beams (3 beam pairs)
Footprint Diameter	$\sim 25$ m	$\sim 17$ m
Along-Track Spacing	$\sim 60$ m between shots	$\sim 0.7$ m between shots
Across-Track Spacing	Up to $\sim 600$ m	$\sim 3$ km between beam pairs
Vertical Accuracy	$\lesssim 1$ m (typical)	$\lesssim 10$ cm (optimal)
Horizontal Accuracy	$\pm 9$ m	$\pm 6.5$ m
Revisit Cycle	Varies with ISS orbit	$\sim 91$ days ground-track repeat
Primary Focus	Forest structure & carbon dynamics	Land/sea ice, vegetation, global terrain

#### 4.2.1. Comparison with GEDI

Although both GEDI and ICESat-2 offer sparse yet precise LiDAR measurements, their coverage, orbit, and revisit cycles differ substantially. Table 1 provides an overview of core specifications, while Figure 4 summarizes ICESat-2's mission highlights. GEDI, hosted on the International Space Station (ISS), was designed primarily for forest canopy and biomass studies (Dubayah et al., 2022; Qi and Dubayah, 2016; Schneider et al., 2020; Shendryk, 2022), limiting its latitude coverage to about  $\pm 51^\circ$  and yielding larger gaps between adjacent laser footprints. By contrast, ICESat-2 operates in a dedicated orbit that extends up to  $\pm 88^\circ$  latitude, making it more suitable for near-global terrain mapping.

#### 4.2.2. Why ICESat-2 for Height Calibration

ICESat-2 offers three principal advantages over alternative LiDAR missions for large-scale MHE calibration:

1. **Near-Global Coverage.** ICESat-2 spanning  $\pm 88^\circ$  latitude, provides reference measurements across diverse regions, including high-latitude areas outside GEDI's range.
2. **High Vertical Accuracy.** Under optimal conditions, the ICESat-2 ATL03 photon-level data can achieve sub-decimeter accuracy, allowing robust anchoring of model-predicted heights.
3. **Improved Geolocation.** Beam footprints possess a horizontal geolocation accuracy of about  $\pm 6.5$  m, facilitating reliable alignment with reference imagery or synthetic predictions.

Photon returns are further classified (e.g., ground vs. canopy), aiding the separation of building rooftops from tree crowns—a feature invaluable for urban terrain mapping and 3D modeling tasks.

#### 4.2.3. Relevant Data Products

ICESat-2's ATLAS instrument generates several data products critical for height validation:

- **ATL03 (Global Geolocated Photon Data).** The Level-1B product that stores precise latitude, longitude, and height for each photon return. Flags for signal

vs. background photons help filter valid returns, and instrument/platform corrections (e.g., orientation) are already applied.

- **ATL08 (Land and Vegetation Height).** A Level-3B product derived mainly from ATL03, focusing on terrain and canopy structure at segment intervals. It includes estimated ground elevation and various canopy metrics, assisting in segregating vegetation from the bare Earth surface.

These products, despite their sparse sampling, provide high-fidelity *control points* that can identify and correct systematic offsets in model-based height predictions. The next section (Section 5) explains how to fuse such sparse LiDAR measurements with dense MHE outputs, leveraging a machine-learning-based pipeline to deliver more accurate and consistent nDSM at scale.

## 5. Proposed Calibration Pipeline

This section explains how NASA's ICESat-2 mission data are utilized to calibrate the height predictions obtained from MHE model. Figure 5 illustrates the overall workflow. First, we address the high complexity and noise in the raw ICESat-2 data by applying a thorough preprocessing pipeline to produce a "clean" subset of photon returns (§5.1–§5.4). Next, these refined data are used in conjunction with low-level image features extracted from the MHE model's encoder to train a random forest model (Breiman, 2001) (§5.6–§5.7). Finally, the trained model is applied across the entire region of interest to generate a dense, calibrated height map. In the sections that follow, we describe each stage of this pipeline in detail: from photon retrieval and geolocation offset correction to land-cover-aware filtering, feature extraction, and residual-based random forest regression.

### 5.1. Photon Data Acquisition and Preprocessing

NASA's ICESat-2 mission provides two principal products relevant to our calibration approach:

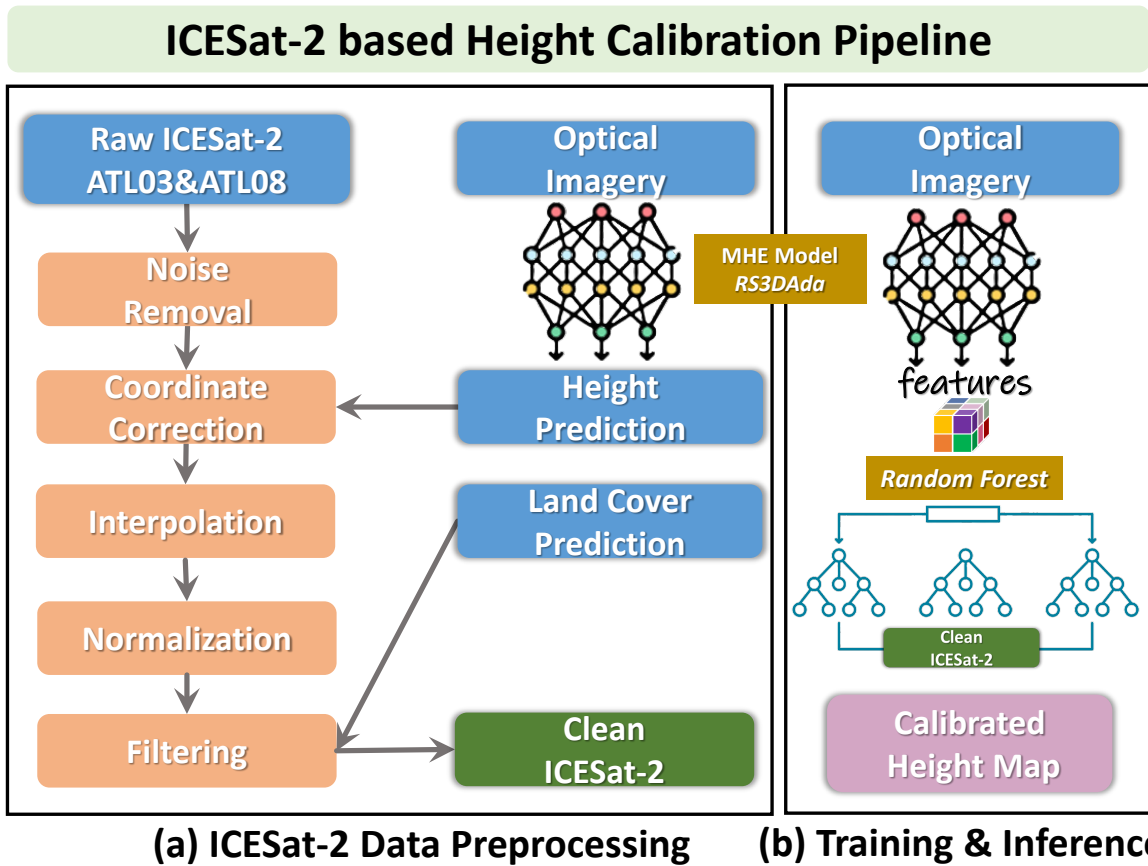


**Figure 5:** Overview of the two-step workflow. The left portion (a) illustrates the ICESat-2 data preprocessing pipeline, while the right portion (b) shows the subsequent calibration stage using a random forest model.

1. **ATL03 (Global Geolocated Photons):** Contains all photons (signal and noise) with per-photon geolocation and confidence attributes. The `signal_conf` values range from  $-2$  (instrumental artifacts) to  $4$  (highest confidence).
2. **ATL08 (Land and Vegetation Height):** Extends ATL03 by classifying each photon into broader surface categories such as *ground*, *canopy*, and *top of canopy*.

**Retrieval via SlideRule.** To efficiently query ICESat-2 data, we use the SlideRule<sup>7</sup> Python library, which provides an interface to the ICESat-2 resources, returning geolocated photon data along with related metadata. By setting parameters like `srt= 3`, `cnf= 0`, and `quality_ph= 0`, SlideRule avoids photons flagged as instrumental artifacts. Numerically, confidence levels  $3$  (medium) and  $4$  (high) correspond to the most reliable ATL03 photons; hence, only these are retained for further processing.

**Combining ATL03 with ATL08 Classification.** For more advanced photon classification, we specify:

<sup>7</sup><https://github.com/ICESat2-SlideRule/sliderule-python>

- `atl08_class = {atl08_ground, atl08_canopy, atl08_top_of_canopy}`<sup>8</sup>,

so that each photon is aligned with these surface categories. Including ATL08 ensures that we retain only photons labeled as legitimate terrain surfaces (ground) or above-ground surfaces (canopy/top of canopy), discarding those classified as noise or unclassified.

**Initial Photon Refinement.** The combined dataset undergoes the following coarse filtering:

1. **ATL03 Confidence Threshold:** Any photon with a `signal_conf` below  $3$  is removed to exclude low-confidence or background noise photons.
2. **ATL08 Classification Filter:** Photons must be classified as `atl08_ground`, or `atl08_top_of_canopy` to be retained, discarding spurious returns (e.g., atmospheric noise).

As shown in Figure 6, although this initial filtering step is not highly precise, it provides a crucial baseline for subsequent calibration. By combining ATL03 and ATL08 filtering, we obtain a refined photon subset that reliably

<sup>8</sup>While these classes are often labeled as “vegetation” categories, they can also include other non-ground returns, such as buildings or other elevated surfaces.

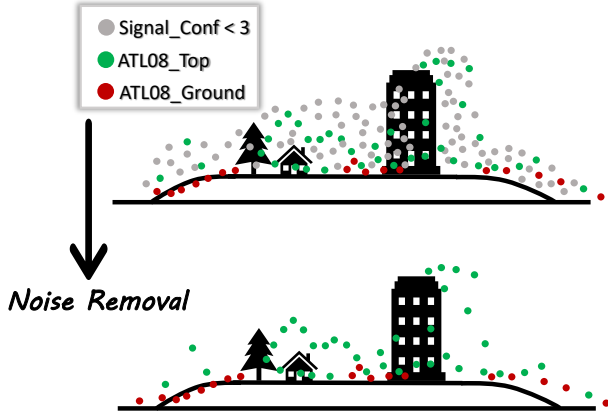


**Figure 6:** Illustration of the ICESat-2 denoising process. The top panel shows the raw photon returns, while the bottom panel depicts the data after the initial denoising step.

represents terrain or above-ground surfaces, forming the foundation for further height calibration.

## 5.2. Hierarchical Horizontal Offset Correction

**Motivation and Rationale.** On-orbit alignment errors and time-varying pointing biases in the ATLAS laser instrument can degrade the horizontal positioning accuracy of ICESat-2 photon returns (Agca et al., 2024; Brunt et al., 2019; Magruder et al., 2021a,b; Wang et al., 2019). While the mission specification allows for up to 6.5 m of horizontal error (Luthcke et al., 2005; Neumann et al., 2019), actual offsets can vary from pass to pass depending on orbit ephemeris solutions, attitude control, calibration drifts, and data product updates. Such horizontal displacement  $\sigma_h$  can induce a vertical elevation error  $\sigma_v$  on sloped terrain, approximated by:

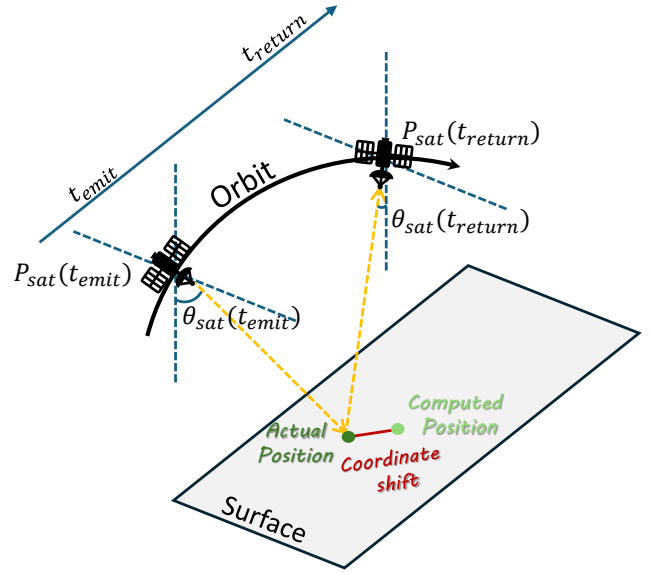
$$\sigma_v = \sigma_h \tan(\alpha), \quad (1)$$

where  $\alpha$  is the local slope angle (Gao et al., 2023b). On a 30° slope, a 6.5 m horizontal error can translate into a vertical error of about 3.76 m.

**Causes of Horizontal Shifts.** Geolocation of photon returns involves a detailed calculation of:

- Satellite orbital position and velocity (ephemeris) at emission and reception times,
- Laser pointing angles and attitude control (pitch, roll, yaw),
- Time-of-flight measurements, calibration, and atmospheric corrections,
- Earth rotation, reference frame transformations, geophysical models, etc.

Figure 7 illustrates how small uncertainties in these factors lead to an offset between the actual ground bounce point (dark green) and the computed position from the ATL03



Small error of  $\Delta P_{sat}$ ,  $\Delta \theta_{sat}$ ,  $\Delta t$  cause large coordinate shift.

**Figure 7: Schematic of ICESat-2 coordinate shifts.** Tiny errors in orbit, attitude, and timing can result in a meter-scale offset (dark green vs. light green) on the ground.

product (light green). In simplified form, assuming near-nadir pointing, the ground intersection  $\mathbf{P}_{ground}$  can be written:

$$\mathbf{P}_{ground} = \mathbf{P}_{sat}(t_{emit}) + [\Delta R(\dots)] \hat{\mathbf{d}}, \quad (2)$$

where  $\Delta R$  is the one-way range from round-trip travel time (with instrumental and atmospheric corrections), and  $\hat{\mathbf{d}}$  is the unit direction vector derived from satellite attitude. In reality, additional parameters (e.g., reference ellipsoid or geoid models) (Neumann et al., 2018) further refine  $\mathbf{P}_{ground}$ .

**Offset Correction Approach.** In applications involving steep terrain or high-resolution image matching, even a few meters of horizontal shift can cause significant errors and misalignment (Gao et al., 2023b). To mitigate this, we leverage the pixel-level surface height predictions from the MHE model (assumed to have negligible horizontal bias). We then perform a two-stage grid search over potential horizontal offsets ( $\Delta x$ ,  $\Delta y$ ), shifting the ATL03 photon coordinates to match these predicted elevations. By minimizing discrepancies between the MHE model's prediction and ICESat-2 photon heights along track, we reduce horizontal misalignments, improve consistency across datasets, and ultimately enhance the accuracy of the derived elevation measurements.

**Offset Definition.** Let  $(x_i, y_i)$  denote the original coordinates of each photon  $i$  in our dataset. We introduce an offset  $(\Delta x, \Delta y)$  that translates every photon by

$$(x'_i, y'_i) = (x_i + \Delta x, y_i + \Delta y). \quad (3)$$

We subsequently recalculate the photonic normalized and filtered height  $h'_i$  at the shifted coordinates  $(x'_i, y'_i)$  using the methods described in Section 5.3 and Section 5.4 (e.g., IDW-based ground interpolation). This yields a shifted point cloud that can be quantitatively compared against a reference raster.

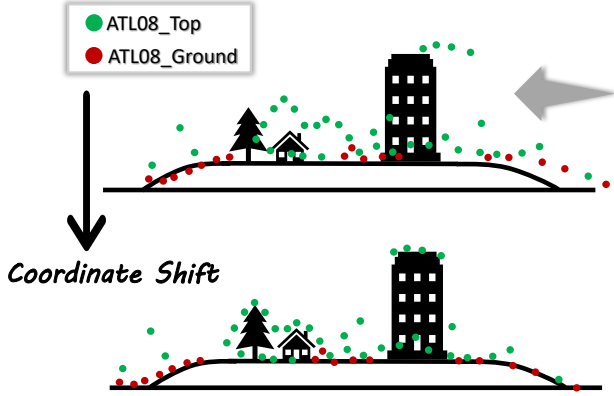


**Figure 8:** Illustration of the ICESat-2 coordinate correction. The top panel shows the data before correction, while the bottom panel shows the data after correction.

**Cost Function.** To measure alignment quality, we evaluate the MAE or RMSE between the shifted photon-based  $n$ DSM heights and the ground-truth raster  $n$ DSM:

$$\text{MAE}(\Delta x, \Delta y) = \frac{1}{N} \sum_{i=1}^N \left| h'_i - \hat{H}(x'_i, y'_i) \right|, \quad (4)$$

$$\text{RMSE}(\Delta x, \Delta y) = \sqrt{\frac{1}{N} \sum_{i=1}^N \left( h'_i - \hat{H}(x'_i, y'_i) \right)^2}, \quad (5)$$

where  $\hat{H}(x'_i, y'_i)$  denotes the ground-truth height sampled from the MHE model predicted  $n$ DSM at the shifted photon location  $(x'_i, y'_i)$ . The goal is to find  $(\Delta x, \Delta y)$  that minimizes these error metrics.

**Coarse-to-Fine Search.** In practice, we bound the horizontal search range to  $\pm 6.5$  m around an initial guess of  $(0, 0)$ :

1. **Coarse Grid:** We sample a range of offsets in integer increments (e.g., 1.0 m), producing a coarse grid of candidate  $(\Delta x, \Delta y)$  points. For each candidate, the entire photon set is shifted according to Equation (3), and the error in Equation (5) is computed. The offset yielding the lowest error is selected as the “coarse best.”
2. **Fine Grid:** Centered on the coarse best offset, we refine  $(\Delta x, \Delta y)$  in finer steps (e.g., 0.1 m) within a smaller bounding box (e.g.,  $\pm 1.0$  m around the coarse best). This more granular search provides sub-meter precision in identifying the final offset that minimizes height misalignment.

**Algorithmic Sketch.** An outline for the hierarchical offset correction follows:

1. **Initialize:** Set maximum allowable shift  $\Delta_{\max} \approx 6.5$  m.
2. **Coarse Search:**
  - (a) Generate  $\{(\Delta x, \Delta y)\}$  on a 1.0 m grid within the range of  $[-\Delta_{\max}, +\Delta_{\max}]$ .
  - (b) Translate all photons and compute RMSE (or MAE).
  - (c) Retain the  $(\Delta x, \Delta y)$  that provides the lowest error.
3. **Fine Search:**
  - (a) Center a smaller search window around the best coarse offset.
  - (b) Refine in 0.1 m increments, retaining the offset that minimizes the cost function.

This hierarchical scheme balances computational efficiency with spatial precision. It successfully corrects for the observed  $\pm 6.5$  m offsets in ICESat-2 data, enabling improved alignment of photon-based height measurements and the reference  $n$ DSM.

As shown in Figure 8, by applying a systematic grid search over potential horizontal displacements, we can identify and correct the intrinsic geolocation shift in ICESat-2 photon data. This refined alignment reduces discrepancies between the photon-derived heights and external ground-truth references, it serves primarily as an intermediate step in our height calibration pipeline.

### 5.3. Normalization via Ground-Point Interpolation

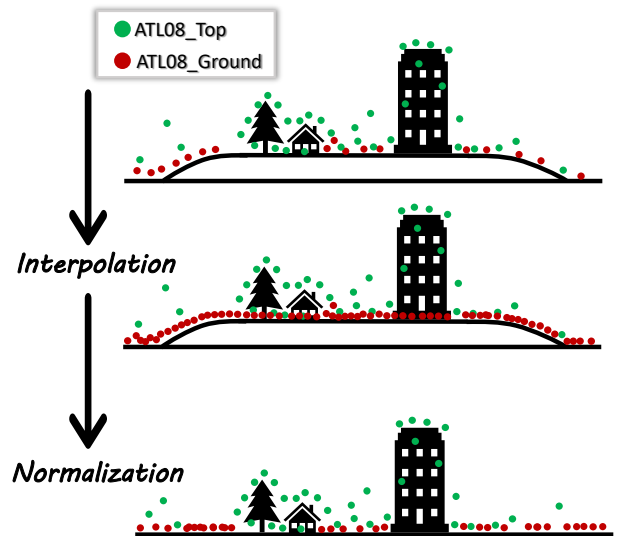


**Figure 9:** Overview of the normalization procedure. The top panel shows the results obtained from the previous step, the middle panel illustrates the ground interpolation process, and the bottom panel depicts the final normalized heights.

As shown in Figure 9, once a photon’s horizontal coordinates have been properly aligned (Section 5.2), the next

essential step is to *normalize* each photon's height relative to the local ground surface. Specifically, photons originating from *ground* returns (`atl08_class = 1`) carry valuable information about the bare-earth elevation—commonly referred to as a Digital Terrain Model (DTM). Meanwhile, photons from *canopy* or *top-of-canopy* classes (`atl08_class ∈ {2, 3}`) correspond more closely to the Digital Surface Model (DSM). To isolate above-ground height (or nDSM), we estimate the local ground elevation at each canopy-photon coordinate and subtract this value from the canopy photon's raw elevation.

**Normalized Digital Surface Model.** Let  $h_{\text{ground}}(x, y)$  be the ground-surface height at  $(x, y)$ , and let  $h_{\text{photon}}(x, y)$  be the observed photon height at the same location. Then the normalized surface height,

$$h_{\text{nDSM}}(x, y) = h_{\text{photon}}(x, y) - h_{\text{ground}}(x, y), \quad (6)$$

captures the vertical extent above bare earth. For ground photons,  $h_{\text{ground}}(x, y)$  approximately equals  $h_{\text{photon}}(x, y)$ ; hence,  $h_{\text{nDSM}}(x, y)$  is zero, while for canopy photons it is strictly positive.

**Ground-Height Interpolation.** A critical subtask is to estimate  $h_{\text{ground}}(x, y)$  at arbitrary canopy-photon locations using only sampled ground photons. Denote the set of ground points by  $\{(x_i, y_i, z_i)\}_{i=1}^G$ , where each  $z_i$  is the measured elevation of a ground photon. Common interpolation schemes include:

1. **Inverse Distance Weighting (IDW)** (Shepard, 1968):

$$\hat{z}(x, y) = \frac{\sum_{i=1}^K \omega_i z_i}{\sum_{i=1}^K \omega_i}, \quad \omega_i = \frac{1}{\|\mathbf{p} - \mathbf{p}_i\|^p}, \quad (7)$$

where  $\mathbf{p} = (x, y)$ ,  $\mathbf{p}_i = (x_i, y_i)$ ,  $p$  is a distance exponent (often set to 2), and  $K$  is the number of nearest ground samples.

2. **Radial Basis Functions (Spline)** (Buhmann, 2000):

$$\hat{z}(x, y) = \sum_{i=1}^G \alpha_i \phi(\|\mathbf{p} - \mathbf{p}_i\|), \quad (8)$$

with  $\phi$  specifying a radial kernel (e.g., linear or thin-plate) and  $\alpha_i$  as fitted coefficients.

3. **Kriging** (OLIVER and WEBSTER, 1990): A geostatistical method modeling spatial covariance and providing both an estimate and an error variance at each location.

All these methods rely on known ground photons to infer  $h_{\text{ground}}$  at canopy points. To balance the speed and accuracy trade-off, we use IDW in our implementation, which enabling a robust nDSM computation of Equation (6).

**Implementation Notes.** A minute *jitter* is added to ground-photon coordinates to prevent numerical issues if multiple photons share identical  $(x, y)$  positions. Once each canopy photon's ground height  $\hat{z}(x, y)$  is interpolated, we update  $h_{\text{nDSM}} = h_{\text{photon}} - \hat{z}(x, y)$ . Ground photons are directly set to 0. Finally, any negative  $h_{\text{nDSM}}$  values, arising from slight inaccuracies or misclassifications, are discarded as unphysical. This ensures only positive (above-ground) canopy heights remain for subsequent calibration steps.

## 5.4. Land-Cover-Aware Photon Filtering and Interpolation

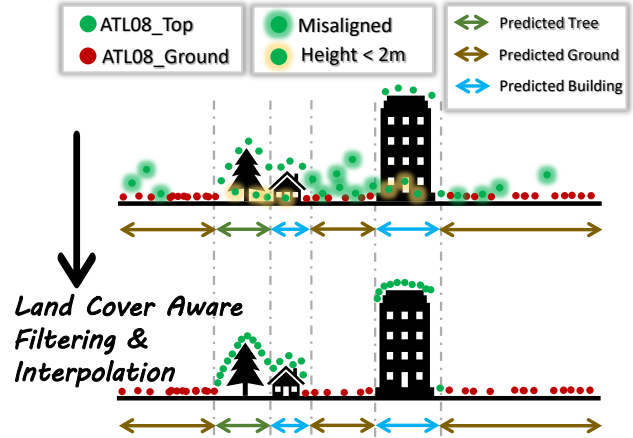


**Figure 10:** Overview of the land-cover-aware filtering process for ICESat-2. The top panel shows the normalized photon data, while the bottom panel depicts the final cleaned ICESat-2 data, ready for downstream training. The predicted classes are from the land cover mapping branch of the MHE model.

**Motivation.** While the ATL08 classification provides a preliminary categorization of photons (e.g., ground versus canopy), its granularity and accuracy can be limited (Feng et al., 2023; Markus et al., 2017; Neuenschwander and Pitts, 2019; Tian and Shan, 2021). To further refine the set of usable photons, we leverage a separate land-cover product predicted by the state-of-the-art MHE model—RS3DAda (Song et al., 2024a). By harmonizing these classifications with the ATL08 labels, we discard unlikely or inconsistent photon returns and, where data are sparse, interpolate missing values within above-ground land-cover category.

**Grid-Based Partition.** We first subdivide the study region into grid cells of size  $GSD \times GSD$  (e.g., 0.5 m). For each photon  $\mathbf{p}_i = (x_i, y_i)$ , the coordinates are rounded to the nearest grid-cell center,

$$(\tilde{x}_i, \tilde{y}_i) = \left( \text{round}\left(\frac{x_i}{GSD}\right) \times GSD, \text{round}\left(\frac{y_i}{GSD}\right) \times GSD \right).$$

All photons assigned to the same  $(\tilde{x}, \tilde{y})$  form one “cell group.”

**Dominant Land Cover.** Within each cell group, we identify the most frequent land-cover class based on MHE

model’s predictions (e.g., *ground*, *tree*, *building*). Because both MHE model’s and ATL08 classifications can be imperfect, we retain only those photons that exhibit *consistent* labeling across both sources. Concretely:

- **Ground:** If MHE model indicates *ground* and ATL08 reports `atl08_class = 1`, these photons are taken as valid ground measurements. Their  $h_{\text{nDSM}}$  values are set to zero, preserving a reliable terrain reference.
- **Tree or Building:** If MHE model assigns *tree* or *building* and ATL08 labels the photon as canopy (`atl08_class ∈ {2, 3}`), we aggregate the corresponding  $h_{\text{nDSM}}$  values (e.g., by a mean) to yield a single representative canopy/building height for that grid cell. We also apply an additional height threshold to ensure only sufficiently tall structures are classified as buildings or trees.

Any photons for which MHE model and ATL08 are in conflict (e.g., *tree* vs. *ground*) are discarded. This mutual-consistency filter further improves data quality by eliminating erroneous classifications from either source.

**Interpolation in Sparse Regions.** Some grid cells may contain minimal or no usable photons. For these cells, we again perform an IDW (Shepard, 1968) interpolation according to the Equation (7). This ensures that large gaps in photon coverage (e.g., building courtyards or canopy patches) do not produce voids in the final dataset.

**Clean Photon Reference.** As shown in Figure 10, by applying land-cover-aware filtering and interpolation, we obtain a cleaner, more coherent set of photon heights suitable for downstream calibration. This process discards evidently misplaced photon returns, aligns the retained heights with the expected land-cover semantics, and fills local voids via IDW interpolation. The end result is a more robust and uniform sampling of photon-derived nDSM values across ground, trees, and buildings.

## 5.5. Before Preprocessing vs. After Preprocessing

As illustrated in Figure 11, the difference between the unprocessed data (left column) and the fully processed data (right column) is immediately apparent in both the scatter plots (top) and the residual histograms (bottom). Prior to preprocessing, there is a considerable spread in the photon-derived heights (Figure 11 (a)), resulting in a relatively high RMSE (4.96 m) and even a negative coefficient of determination ( $R^2 = -0.02$ ). By contrast, after applying the proposed pipeline, the point cloud exhibits a much tighter clustering around the one-to-one line (Figure 11 (b)), accompanied by marked improvements in MAE (from 2.55 m to 0.89 m), RMSE (from 4.96 m to 2.57 m), and  $R^2$  (from  $-0.02$  to 0.70). The residual histograms (Figures 11 (c) and 11 (d)) likewise confirm the shift toward smaller, more tightly distributed errors. Altogether, these results underscore the effectiveness of the preprocessing steps in producing cleaner, more reliable photon-height estimates that serve as a stronger basis for subsequent calibration.

## 5.6. Feature Extraction from Optical Imagery

**Motivation and Architecture.** To incorporate visual cues (e.g., color, texture, shadows) into the height calibration process, we extract shallow-layer features from the optical image via the MHE model’s encoder. The encoder adopts a ViT-L architecture (Dosovitskiy et al., 2020), chosen for its strong representational capacity. However, rather than using high-level (late) semantic layers, we retrieve features from an *earlier* layer, as these shallow representations better capture low-level visual patterns (Zeiler, 2014) that strongly correlate with height phenomena such as building edges or vegetation crowns.

**Patch-Wise Feature Embedding.** We subdivide the re-projected optical image into  $14 \times 14$  patches to align with the ViT-L patch resolution. For each patch, the model outputs a feature vector of dimension  $d = 1024$ . Formally, let  $\mathbf{I} \in \mathbb{R}^{H \times W \times 3}$  be the optical image and  $f_\theta$  the ViT-L encoder truncated at an intermediate block. We obtain:

$$\mathbf{F} = f_\theta(\mathbf{I}) \in \mathbb{R}^{\left(\frac{H}{14} \times \frac{W}{14}\right) \times d}, \quad (9)$$

where each row of  $\mathbf{F}$  corresponds to one patch in  $(H/14) \times (W/14)$  patch layout. Next, for every ICESat-2 photon at location  $(x, y)$ , we map its coordinates to the matching patch index (according to row-column partitioning) and retrieve the associated feature vector  $\mathbf{F}_{(x,y)}$ .

**Photon-Specific Features as Training Input.** By binding each photon’s geolocation to the spatially closest patch, we augment the photon dataset with a robust  $d$ -dimensional embedding of color, texture, and lighting context. These per-photon features furnish valuable cues to help distinguish whether local height discrepancies arise from actual topographic structures, vegetation, or shadow-induced artifacts.

## 5.7. Random Forest-Based Residual Regression

**Residual Definition.** Let  $h_{\text{pred}}(x, y)$  denote the MHE model’s predicted height at  $(x, y)$  and  $h_{\text{photon}}(x, y)$  the clean photon height (Section 5.4). For each photon  $i$ , we define a residual:

$$r_i = h_{\text{pred}}(x_i, y_i) - h_{\text{photon}}(x_i, y_i). \quad (10)$$

This residual encapsulates how far the prediction deviates from the ICESat-2 measurement. We collect all  $\{\mathbf{F}_i, r_i\}$  pairs into a training set, where  $\mathbf{F}_i$  is the feature vector extracted at photon  $i$ ’s patch.

**Training and Inference.** A Random Forest (Breiman, 2001) regressor  $g(\cdot)$  is trained to map each feature vector  $\mathbf{F}_i$  to the residual  $r_i$ . Once fitted, the regressor can be evaluated at any patch on the entire imagery:

$$\hat{r}(x, y) = g(\mathbf{F}_{(x,y)}), \quad (11)$$

yielding a *residual map* over all pixels. The final *corrected height* map thus becomes

$$h_{\text{corr}}(x, y) = h_{\text{pred}}(x, y) - \hat{r}(x, y). \quad (12)$$

## ICESat-2 Vertical Accuracy: Before vs After Preprocessing

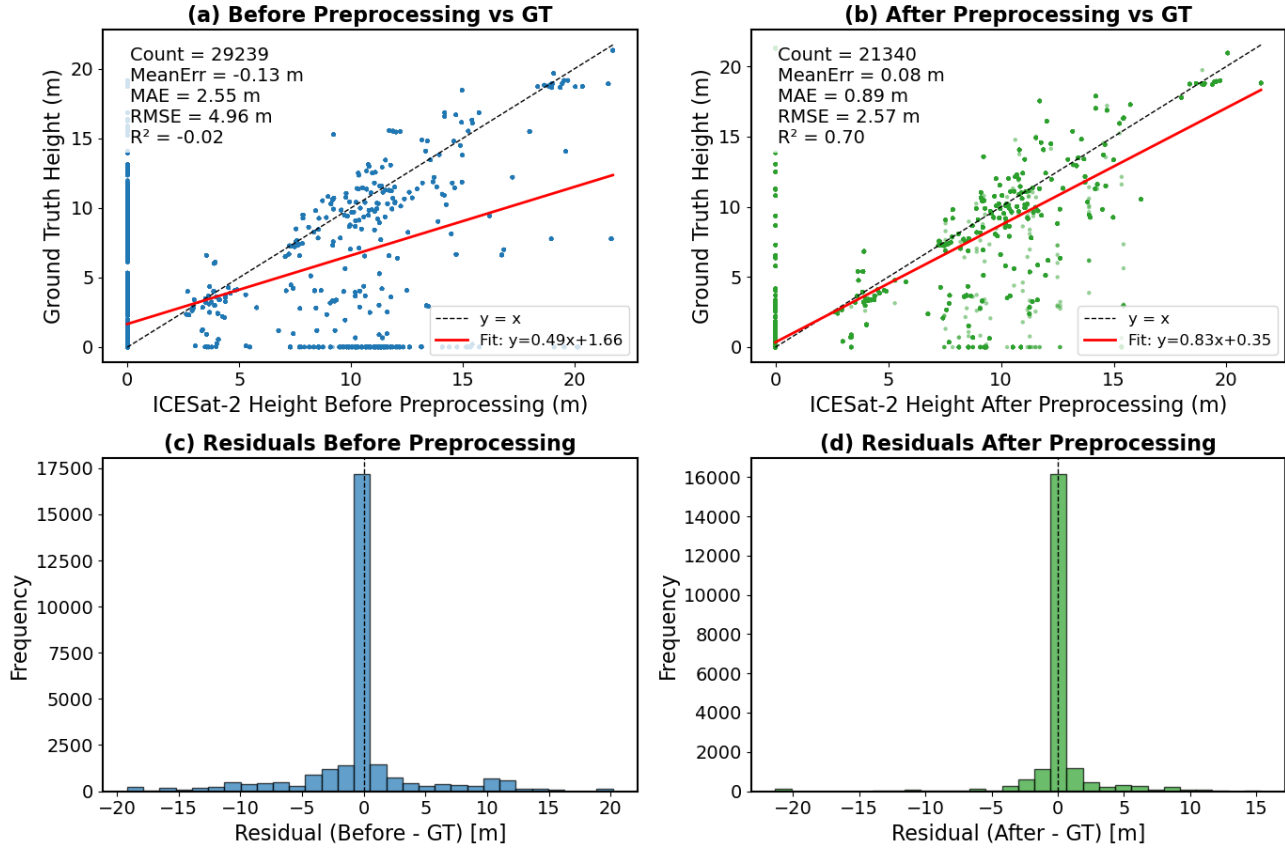


**Figure 11: Saint-Omer, France. ICESat-2 Vertical Accuracy: Before vs. After Preprocessing.** (a) Scatter plot of unprocessed photon-derived heights versus ground truth (GT), (b) scatter plot of processed photon-derived heights versus GT, (c) histogram of residuals before preprocessing, and (d) histogram of residuals after preprocessing. The substantial reduction in MAE and RMSE, as well as the increase in  $R^2$ , illustrate the benefit of our land-cover-aware filtering, geolocation offset correction, and normalization.

Regions where the random forest has sufficient training coverage (e.g., buildings) benefit from a more precise correction.

**Tree-Class Exemption.** In practice, ICESat-2 ground tracks may insufficiently cover tree canopies, leading to data imbalance. Moreover, large within-class variation in building heights (e.g., 6 m versus 60 m structures) contrasts with the comparatively narrower range for most tree canopies in a localized area. We therefore *retain* the original prediction for pixels classified as *tree*. In other words, for any  $(x, y)$  predicted as *tree*, we skip the residual-based correction and preserve  $h_{\text{pred}}(x, y)$  directly. Empirically, this approach has shown to mitigate overcorrection of vegetative zones while significantly improving building height estimates.

## 6. City-Wide Case Studies

Having established our sparse-data correction method (Section 5), we now demonstrate its effectiveness across three contrasting urban areas: Saint-Omer (France), Tokyo (Japan), and São Paulo (Brazil). This section presents both

quantitative and qualitative analyses of the corrected nDSM results in real-world city environments, illustrating how our pipeline adapts to diverse building typologies, varying heights, and dense development within compact urban cores.

### 6.1. Study Areas and Data Sources

To validate the generalizability of our pipeline, we selected three city regions with publicly available LiDAR-based ground-truth nDSMs and high-resolution optical imagery. Figures 12, 13, and 14 provide an overview of the respective data sources, and Table 2 summarizes key specifications.

- **Saint-Omer, France (Europe):** A mid-sized town with a historical center characterized by moderate building heights and a patchwork of vegetated areas. The optical imagery is from Bing Satellite at 0.5 m ground sampling distance (GSD). The reference nDSM is derived from the IGN Lidar HD project<sup>9</sup> at 0.5 m GSD, collected in early 2023.

<sup>9</sup><https://diffusion-lidarhd.ign.fr/mnx/>

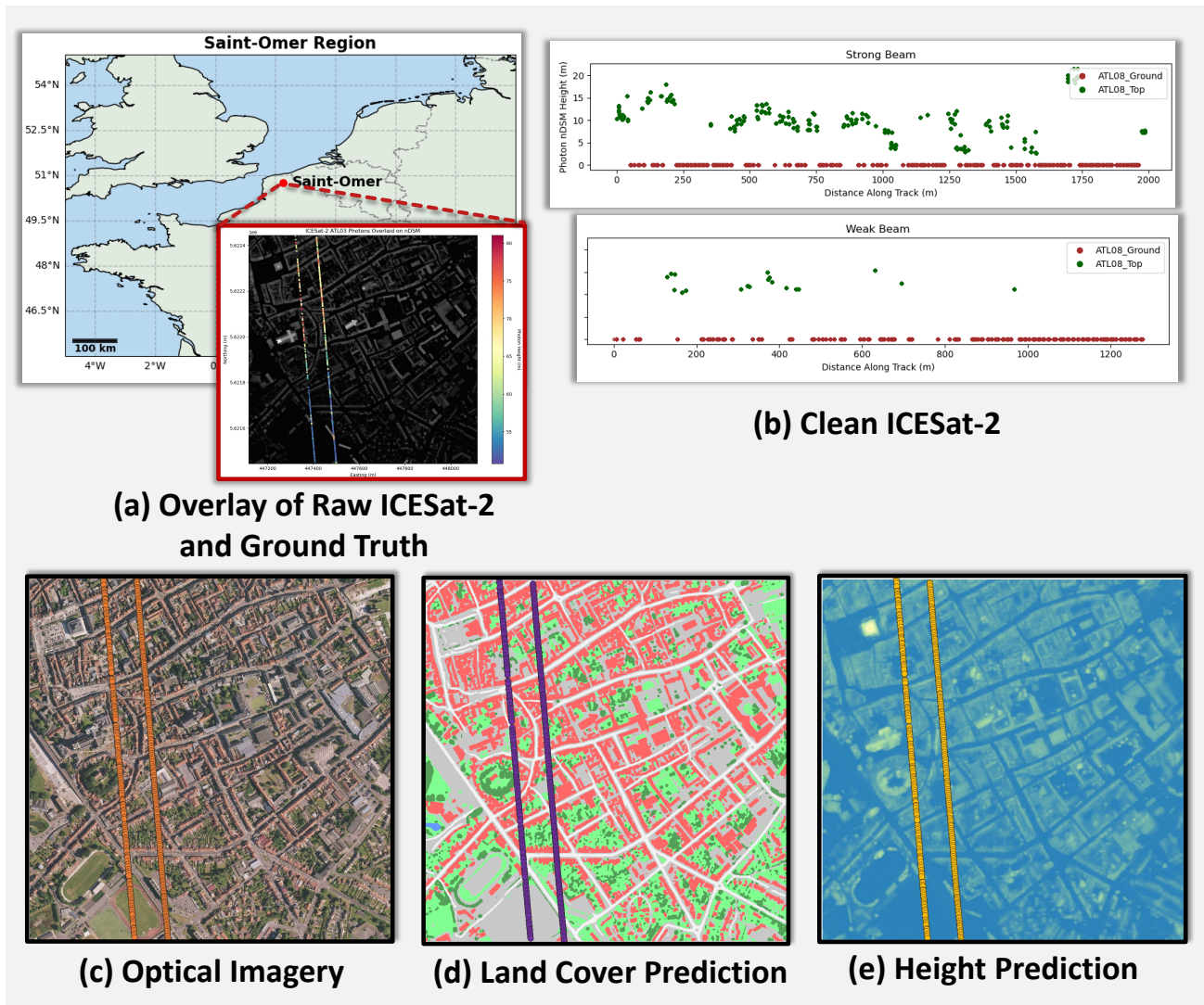


**Figure 12:** All data used for the calibration pipeline in Saint-Omer (France). Subfigures: (a) raw ICESat-2 data, (b) cleaned ICESat-2 returns, (c) optical imagery, (d) MHE land cover prediction, and (e) MHE height prediction. These correspond to the data types in Figure 5.

- **Tokyo, Japan (Asia):** A global megacity with highly heterogeneous building structures, including skyscrapers, mid-rises, and dense residential blocks. Both the optical imagery and ground-truth nDSM (at 0.5 m GSD) are from the Tokyo Digital Twin Project<sup>10</sup> of the Tokyo Metropolitan Government, captured in 2023 (March–April).
- **São Paulo, Brazil (South America):** One of the largest metropolitan areas in Latin America, featuring extensive high-rise clusters, sprawling suburban zones, and mixed residential-commercial districts. We employ LiDAR data released by the São Paulo City Hall through the GeoSampa platform<sup>11</sup> with a point density of  $\sim 10$  points/m<sup>2</sup>. The LiDAR data (DSM

and DTM) collected in 2020 were used to derive a reference nDSM at 0.3 m GSD. Optical imagery (originally 0.1 m GSD) was downsampled to 0.3 m to match the nDSM resolution.

For each study area, we apply the calibration pipeline outlined in Section 5:

1. **Download & preprocess ICESat-2 data** (ATL03, ATL08) using SlideRule, retaining high-confidence photons.
2. **Hierarchical horizontal offset correction** to align photon returns with the MHE model-predicted nDSM.
3. **Normalization** by interpolating bare-earth photons.
4. **Land-cover-aware filtering** to exclude photons that are misaligned or insufficient in height.
5. **Random-Forest regression** on the residual between MHE model's prediction and ICESat-2 above-ground

<sup>10</sup><https://info.tokyo-digitaltwin.metro.tokyo.lg.jp/>

<sup>11</sup>[https://geosampa.prefeitura.sp.gov.br/PaginasPublicas/\\_SBC.aspx](https://geosampa.prefeitura.sp.gov.br/PaginasPublicas/_SBC.aspx)

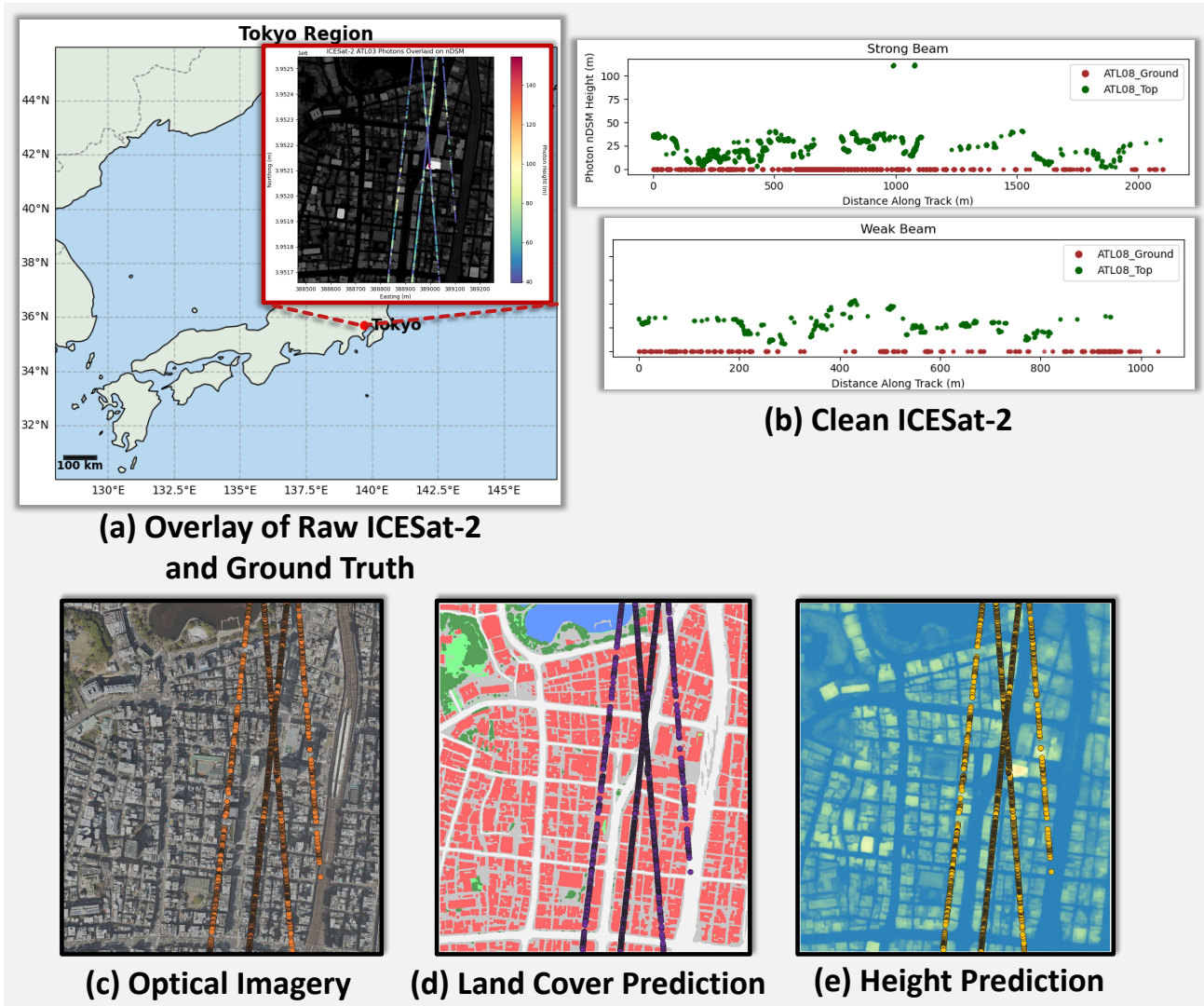


**Figure 13:** All data used for the calibration pipeline in Tokyo (Japan). Subfigures: (a) raw ICESat-2 data, (b) cleaned ICESat-2 returns, (c) optical imagery, (d) MHE land cover prediction, and (e) MHE height prediction. These correspond to the data types in Figure 5.

**Table 2**  
Key data specifications for the three city-wide case studies.

City	Approx. Area	GSD	ICESat-2 Overpass
Saint-Omer (France)	~ 1 km <sup>2</sup>	0.5 m	2022.12.09
Tokyo (Japan)	~ 0.7 km <sup>2</sup>	0.5 m	2021.01.13–2021.12.04
São Paulo (Brazil)	~ 0.4 km <sup>2</sup>	0.3 m	2021.03.04–2021.07.01

heights, guided by shallow-layer MHE model’s features.

## 6.2. Along-Track ICESat-2 Quantitative Evaluation and Discussion

Table 3 compares the Mean Absolute Error (MAE), Root Mean Square Error (RMSE), and the estimated horizontal shifts (in meters) for three datasets in each city: MHE model-based *prediction*, the fully preprocessed *ICESat-2* footprints,

and the *after-calibration* results along the ICESat-2 track. Note that the horizontal shifts for the MHE model’s predictions are effectively zero, because the model operates in a pixel-aligned grid and is thus assumed to be horizontally correct. For ICESat-2, a meter-level coordinate shift is found and corrected. The last row in each city block gives the vertical MAE and RMSE after calibration using along-track photon heights.

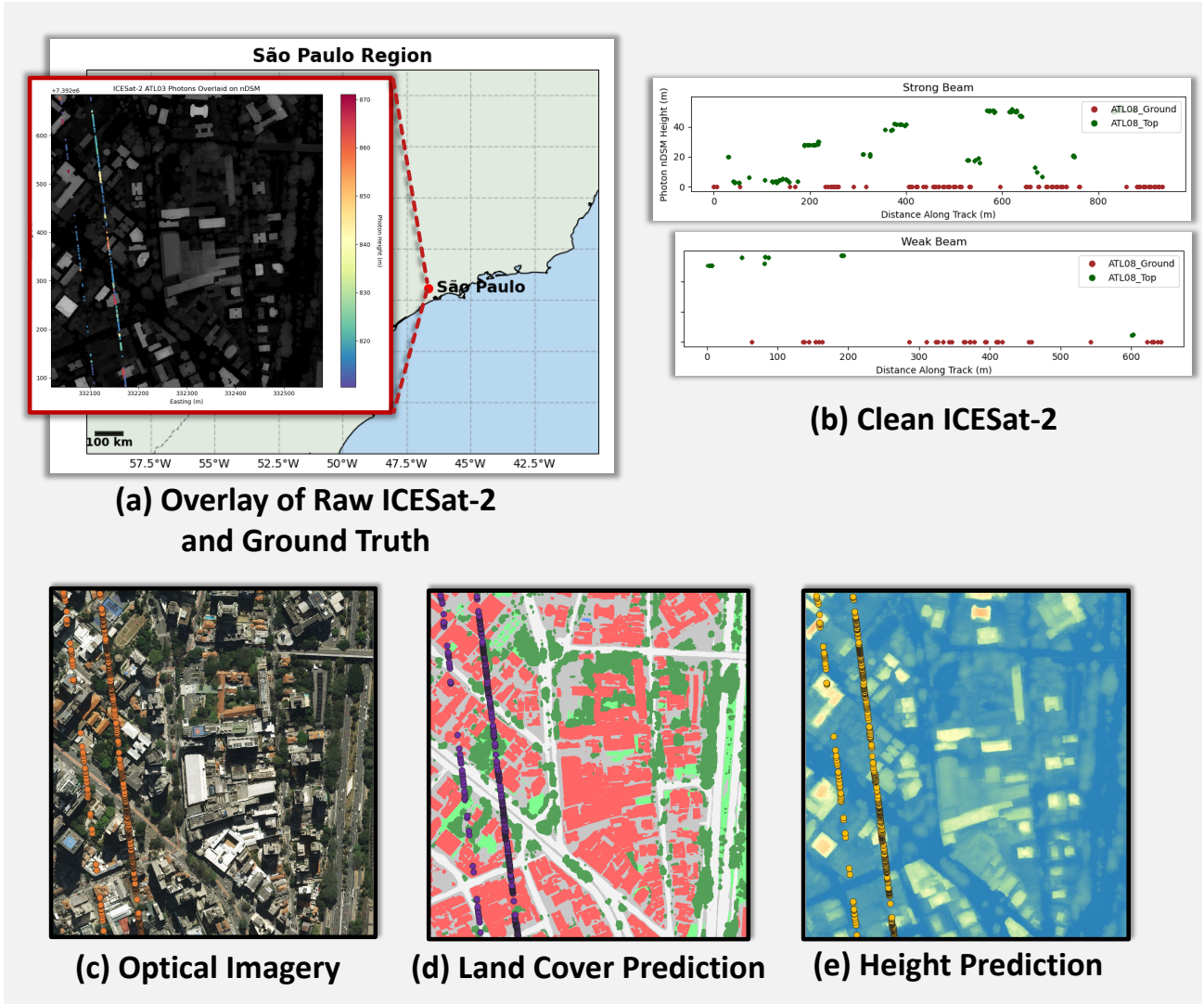


**Figure 14:** All data used for the calibration pipeline in São Paulo (Brazil). Subfigures: (a) raw ICESat-2 data, (b) cleaned ICESat-2 returns, (c) optical imagery, (d) MHE land cover prediction, and (e) MHE height prediction. These correspond to the data types in Figure 5.

**Table 3**

Comparison of vertical accuracy (MAE, RMSE) for the city-wide case studies, based on along-track ICESat-2 data after all preprocessing steps. The columns  $x_{\text{shift}(\text{applied})}$  and  $y_{\text{shift}(\text{applied})}$  (in meters) indicate the horizontal shifts applied to raw ICESat-2 during preprocessing. The final row in each city section shows the *along-track* MAE and RMSE after vertical calibration. Note that these calibration results along the track differ from those reported in Table 4, which presents calibration results for the entire study area.

City	Source (Along-track)	MAE	RMSE	$x_{\text{shift}(\text{applied})}$	$y_{\text{shift}(\text{applied})}$
Saint-Omer	MHE Pred.	1.91	3.37	–	–
	Clean ICESat-2	1.06	2.81	-1.3	1.4
	MHE Pred. After Cali.	1.13	2.80	–	–
Tokyo	MHE Pred.	6.60	11.50	–	–
	Clean ICESat-2	4.91	10.52	-0.8	0.4
	MHE Pred. After Cali.	4.95	9.48	–	–
São Paulo	MHE Pred.	6.01	10.16	–	–
	Clean ICESat-2	4.30	8.70	-1.0	0.6
	MHE Pred. After Cali.	3.63	5.56	–	–

**Target Accuracy.** The overarching goal of our pipeline is to reduce the vertical error of the MHE model-based nDSM estimation to a level comparable with the more precise ICESat-2 vertical measurements, so that the corrected nDSM is suitable for a broad range of applications (e.g., urban planning, flood modeling, and 3D city modeling). As indicated in Table 3, the vertical accuracy of ICESat-2 footprints (with respect to LiDAR ground truth) is generally superior to the raw MHE model’s predictions, motivating our choice to calibrate the latter with ICESat-2 data. Potential end-users include municipal authorities, disaster management agencies, and researchers requiring large-scale 3D urban models. Our objective is to bring the city-scale nDSM predictions closer to the vertical accuracy offered by ICESat-2.

**Horizontal vs. Vertical Errors.** A natural concern is the apparent circularity of using the MHE model’s *estimated* results to *correct* the ICESat-2 footprints horizontally (Section 5.2), and then employing those corrected footprints to calibrate our prediction vertically. To address this, we note that:

- **Horizontal alignment** ( $x$  and  $y$  shifts) is primarily corrected based on MHE model’s prediction, which exhibits minimal to negligible horizontal error because the network operates on a pixel-aligned grid. In other words, each pixel’s prediction is directly registered with the underlying optical imagery, so we treat MHE model’s prediction as *horizontally correct*. This assumption lets us detect and remove systematic horizontal offsets in the ICESat-2 footprints.
- **Vertical correction** leverages the fact that ICESat-2 exhibits superior vertical accuracy (as evidenced by the relatively lower MAE/RMSE in the vertical dimension). Thus, we use the photon heights (once horizontally aligned) to refine the vertical height estimates of MHE model’s predictions.

By distinguishing these two error sources (horizontal offset versus vertical inaccuracy), we can draw on each data source’s strength in its respective dimension. The MHE model’s predictions provide stable horizontal alignment, while ICESat-2’s photon heights provide a trusted reference in the vertical domain. Consequently, this strategy is not circular but rather complementary: each dataset contributes corrections where it is most reliable.

### 6.3. Calibration Results and Analysis

After running the full calibration procedure, we evaluate the corrected nDSMs against the respective LiDAR-based ground-truth references. Figures 15, 16, and 17 provide side-by-side comparisons (before vs. after calibration) for Saint-Omer, Tokyo, and São Paulo, respectively, along with quantitative error metrics. Table 4 lists the corresponding MAE and RMSE.

For each study area, we observe consistent improvements in MAE (reductions of up to 0.56 m) and corresponding decreases in RMSE. Qualitatively, building edges become noticeably sharper, and the model corrects many systematic underestimations of taller structures. In mid-rise historical areas such as Saint-Omer, the correction more accurately captures moderate building heights and yields smoother transitions, as shown in Figure 15.

In the extreme vertical urban environment of Tokyo, as shown in Figure 16, high-rise complexes and skyscrapers pose a challenge due to sparse ICESat-2 coverage and potential photon occlusions. Nonetheless, the corrected results show reduced overall error, indicating the pipeline’s robustness to partial LiDAR sampling. São Paulo, with its mixed-density residential landscapes, also benefits from calibration, as shown in Figure 17, achieving clearer delineation of rooftops and an overall reduction in height bias.

These city-wide case studies underscore the feasibility and effectiveness of our ICESat-2–based calibration approach for large-scale, real-world applications. By integrating sparse yet precise LiDAR returns with deep learning based height predictions, the proposed pipeline successfully mitigates systematic biases, refines building outlines, and increases the overall reliability of model predicted nDSMs. This framework thus paves the way for more confident use of synthetic data trained models in production-level remote sensing tasks involving 3D mapping and urban analysis.

## 7. Limitations and Discussion

In this work, we investigated how a state-of-the-art monocular height estimation (MHE) model trained solely on synthetic data interprets VHR remote sensing imagery. Our controlled experiments revealed that the network relies heavily on shadow cues—an insight that underscores both its potential vulnerability to non-standard illumination conditions and the broader interpretability challenges inherent in MHE. To mitigate these issues and improve the reliability of height predictions, we proposed a sparse LiDAR-based correction pipeline. By integrating globally available yet imperfect ICESat-2 measurements, we achieved notable error reductions (up to 22.8% in MAE) in diverse real-world settings across Saint-Omer, Tokyo, and São Paulo.

Although the proposed sparse LiDAR measurement based correction pipeline substantially improves the MHE model’s height predictions, thereby reinforcing the credibility of deep learning methods trained on synthetic data, several limitations must be acknowledged:

1. **Dependence on ICESat-2 Availability.** The pipeline requires ICESat-2 coverage within the inference or application area. If the target region lacks any ICESat-2 ground tracks, the approach cannot be applied.
2. **Sparse ICESat-2 Returns.** Even when geographic coordinate information is present, the sparse distribution of photon returns can limit their effectiveness. In some scenarios, the ICESat-2 tracks may not intersect key urban areas or could lie predominantly over

## Saint-Omer, France, Europe

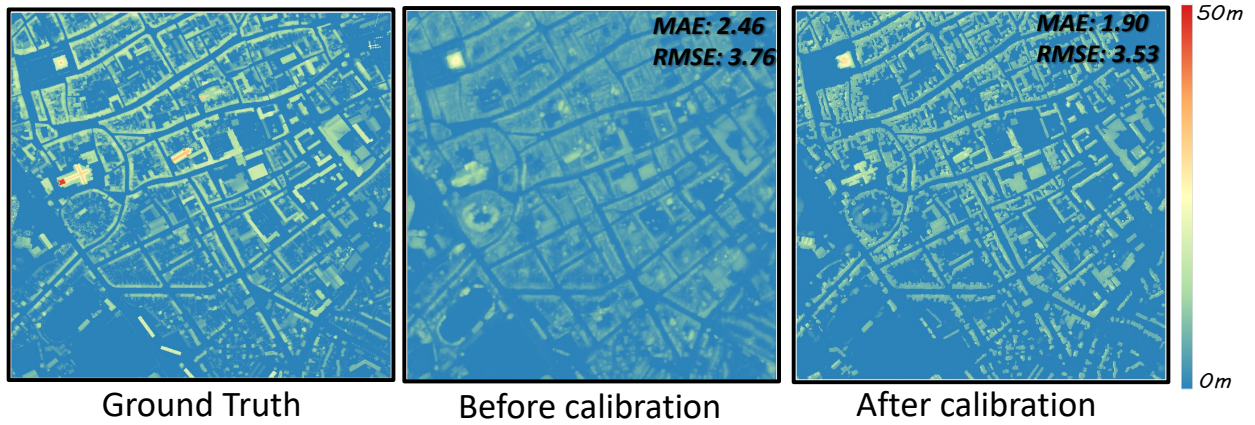


**Figure 15:** Qualitative and quantitative comparison of height maps in Saint-Omer (France). The center image (“Before calibration”) shows the MHE model’s prediction, while the right image (“After calibration”) demonstrates improvements in building delineation and lower overall error.

## Tokyo, Japan, Asia

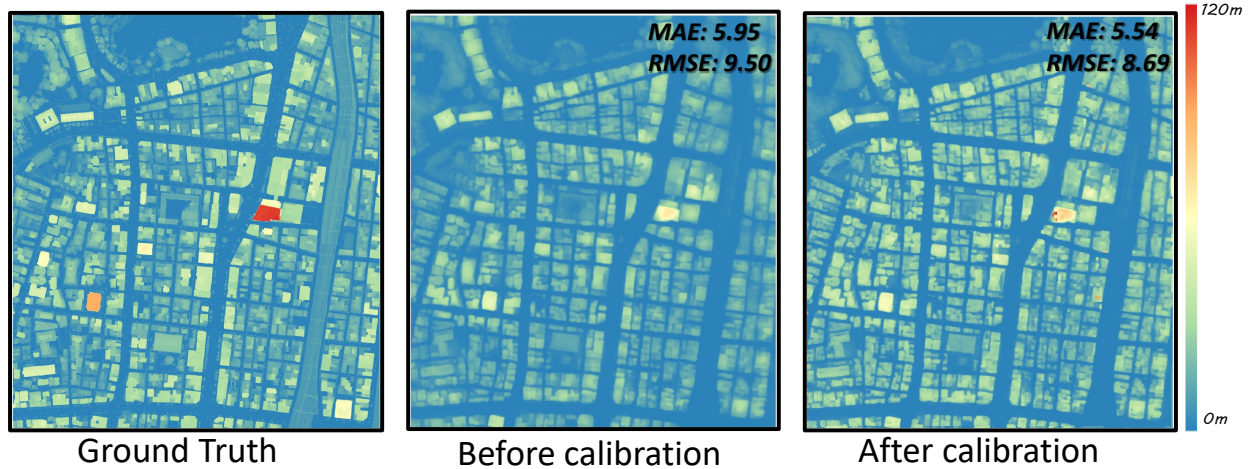


**Figure 16:** Case study results for Tokyo (Japan), illustrating error reductions in high-rise urban environments.

## São Paulo, Brazil, South America

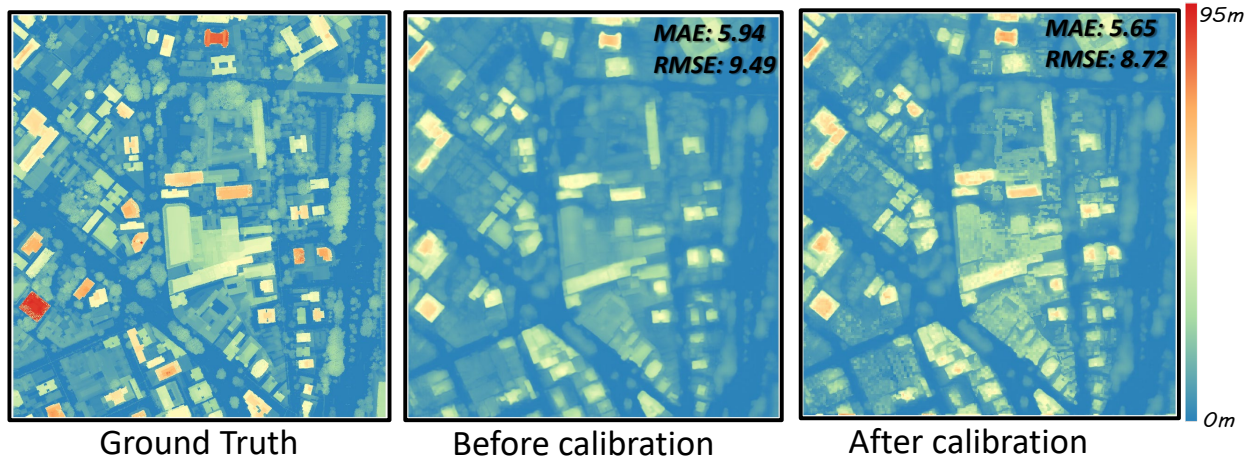


**Figure 17:** Case study results for São Paulo (Brazil), demonstrating improvement in building outlines and urban structures.

**Table 4**

Comparison of pre- and post-correction metrics for each city. MAE and RMSE (in meters) use the “smaller-is-better” convention (indicated by ↓). The “Imp. (%)” column shows the percentage reduction relative to the uncorrected baseline.

City	MAE ↓			RMSE ↓		
	Before	After	Imp. (%)	Before	After	Imp. (%)
Saint-Omer (France)	2.46	1.90	22.8	3.76	3.53	6.1
Tokyo (Japan)	5.95	5.54	6.9	9.50	8.69	8.5
São Paulo (Brazil)	5.94	5.65	4.9	9.49	8.72	8.1

ground or water surfaces, thereby yielding little to no building-related information.

- Influence of Representative Coverage.** The correction results are heavily dependent on how well the available ICESat-2 tracks represent local building structures. If only the periphery of the region is sampled or if high-rise buildings are underrepresented, the corrections may be incomplete or even degrade the original predictions.
- Temporal Discrepancies.** When the time gap between ICESat-2 acquisitions and optical image collection is large, substantial changes in the built environment or natural surfaces may occur. This temporal mismatch reduces the reliability of the correction.
- Processing Overheads.** Although we employ a relatively simple random forest as the final correction model for speed, the preceding photon data preprocessing remains time-consuming. On average, the entire pipeline requires about 2–3 minutes of processing per square kilometer.

Despite these limitations, the global reach and near-real-time potential of the method distinguish it from classical elevation-measurement techniques, such as terrestrial LiDAR, multi-view stereo matching, or InSAR, which may not readily offer equivalent spatial coverage. The simplicity and demonstrated effectiveness of our approach—in which a densely predicted height map is refined through sparse altimetry data—illustrate a promising pathway for future research. By establishing this proof of concept, we hope to inspire more sophisticated methods to build upon the fusion of deep-learning-based surface predictions and sparse LiDAR returns, ultimately advancing large-scale 3D mapping capabilities.

## Acknowledgements

This work was supported in part by JST FOREST Program Grant Number JPMJFR206S; Microsoft Research Asia; JSPS KAKENHI Grant Number 24KJ0652; and the Next Generation AI Research Center of The University of Tokyo.

## References

Agca, M., Yucel, A., Kaya, E., Daloglu, A.İ., Kayalik, M., Yetkin, M., Yalcin, F., 2024. Machine learning algorithms for building height

estimations using icesat-2/atlas and airborne lidar data. *Earth Science Informatics*, 1–12.

- Ameri, B., Goldstein, N., Wehn, H., Moshkovitz, A., Zwick, H., 2002. High resolution digital surface model (dsm) generation using multi-view multi-frame digital airborne images. *INTERNATIONAL ARCHIVES OF PHOTOGRAMMETRY REMOTE SENSING AND SPATIAL INFORMATION SCIENCES* 34, 419–424.
- Bingham, G.P., Pagano, C.C., 1998. The necessity of a perception-action approach to definite distance perception: Monocular distance perception to guide reaching. *Journal of Experimental Psychology: Human Perception and Performance* 24, 145.
- Bourdis, N., Marraud, D., Sahbi, H., 2011. Constrained optical flow for aerial image change detection, in: 2011 IEEE international geoscience and remote sensing symposium, IEEE. pp. 4176–4179.
- Breiman, L., 2001. Random forests. *Machine learning* 45, 5–32.
- Brenner, E., van Damme, W.J., 1999. Perceived distance, shape and size. *Vision research* 39, 975–986.
- Brunt, K., Neumann, T., Smith, B., 2019. Assessment of icesat-2 ice sheet surface heights, based on comparisons over the interior of the antarctic ice sheet. *Geophysical Research Letters* 46, 13072–13078.
- Buhmann, M.D., 2000. Radial basis functions. *Acta numerica* 9, 1–38.
- Chen, H., Song, J., Dietrich, O., Broni-Bediako, C., Xuan, W., Wang, J., Shao, X., Wei, Y., Xia, J., Lan, C., et al., 2025. Bright: A globally distributed multimodal building damage assessment dataset with very-high-resolution for all-weather disaster response. *arXiv preprint arXiv:2501.06019*.
- Chen, S., Shi, Y., Xiong, Z., Zhu, X.X., 2023. Htc-dc net: Monocular height estimation from single remote sensing images. *IEEE Transactions on Geoscience and Remote Sensing* 61, 1–18.
- Dijk, T.v., Croon, G.d., 2019. How do neural networks see depth in single images?, in: *Proceedings of the IEEE/CVF International Conference on Computer Vision*, pp. 2183–2191.
- DLR, 2010. Tandem-x digital elevation model (dem). <https://earth.esa.int/eogateway/missions/terrasar-x-and-tandem-x>. Accessed on 4 March 2025.
- Dosovitskiy, A., Beyer, L., Kolesnikov, A., Weissenborn, D., Zhai, X., Unterthiner, T., Dehghani, M., Minderer, M., Heigold, G., Gelly, S., et al., 2020. An image is worth 16x16 words: Transformers for image recognition at scale. *arXiv preprint arXiv:2010.11929*.
- Dubayah, R., Armston, J., Healey, S.P., Bruening, J.M., Patterson, P.L., Kellner, J.R., Duncanson, L., Saarela, S., Ståhl, G., Yang, Z., et al., 2022. Gedi launches a new era of biomass inference from space. *Environmental Research Letters* 17, 095001.
- Favalli, M., Fornaciari, A., Isola, I., Tarquini, S., Nannipieri, L., 2012. Multiview 3d reconstruction in geosciences. *Computers & Geosciences* 44, 168–176.
- Feng, T., Duncanson, L., Montesano, P., Hancock, S., Minor, D., Guenther, E., Neuenschwander, A., 2023. A systematic evaluation of multi-resolution icesat-2 atl08 terrain and canopy heights in boreal forests. *Remote sensing of environment* 291, 113570.
- Gao, J., Liu, J., Ji, S., 2023a. A general deep learning based framework for 3d reconstruction from multi-view stereo satellite images. *ISPRS Journal of Photogrammetry and Remote Sensing* 195, 446–461.
- Gao, M., Xing, S., Zhang, G., Zhang, X., Li, P., 2023b. Assessment of icesat-2’s horizontal accuracy using an iterative matching method based

- on high-accuracy terrains. *Remote Sensing* 15, 2236.
- Gao, Z., Sun, W., Lu, Y., Zhang, Y., Song, W., Zhang, Y., Zhai, R., 2023c. Joint learning of semantic segmentation and height estimation for remote sensing image leveraging contrastive learning. *IEEE Transactions on Geoscience and Remote Sensing*.
- Garcke, J., Roscher, R., 2023. Explainable machine learning. *Machine Learning and Knowledge Extraction* 5, 169–170. URL: <https://www.mdpi.com/2504-4990/5/1/10>, doi:10.3390/make5010010.
- Ghamisi, P., Yokoya, N., 2018a. Img2dsm: Height simulation from single imagery using conditional generative adversarial net. *IEEE Geoscience and Remote Sensing Letters* 15, 794–798.
- Ghamisi, P., Yokoya, N., 2018b. Img2dsm: Height simulation from single imagery using conditional generative adversarial net. *IEEE Geoscience and Remote Sensing Letters* 15, 794–798.
- Gordon, C., Abujder, R.R.R.M., Foster, K., Hagstrom, S., Hager, G., Brown, M., 2020. Learning geocentric object pose in oblique monocular images, in: *Proceedings of the IEEE Computer Society Conference on Computer Vision and Pattern Recognition*.
- Han, Y., Wang, S., Gong, D., Wang, Y., Ma, X., 2020. State of the art in digital surface modelling from multi-view high-resolution satellite images. *ISPRS Annals of the Photogrammetry, Remote Sensing and Spatial Information Sciences* 2, 351–356.
- Hermosilla, T., Ruiz, L.A., Recio, J.A., Estornell, J., 2011. Evaluation of automatic building detection approaches combining high resolution images and lidar data. *Remote Sensing* 3, 1188–1210.
- Hu, J., Zhang, Y., Okatani, T., 2019. Visualization of convolutional neural networks for monocular depth estimation, in: *Proceedings of the IEEE/CVF international conference on computer vision*, pp. 3869–3878.
- Hu, Z., Hou, Y., Tao, P., Shan, J., 2021. Imgr: Image-triangle based multi-view 3d reconstruction for urban scenes. *ISPRS Journal of Photogrammetry and Remote Sensing* 181, 191–204.
- Huang, X., Cheng, F., Bao, Y., Wang, C., Wang, J., Wu, J., He, J., Lao, J., 2024. Urban building height extraction accommodating various terrain scenes using icesat-2/atlas data. *International Journal of Applied Earth Observation and Geoinformation* 130, 103870.
- JAXA, 2008. Advanced land observing satellite (alos) palsar data. [https://www.eorc.jaxa.jp/ALOS/en/alos/sensor/palsar\\_e.htm](https://www.eorc.jaxa.jp/ALOS/en/alos/sensor/palsar_e.htm). Accessed on 4 March 2025.
- Kolarik, A.J., Moore, B.C., Zahorik, P., Cirstea, S., Pardhan, S., 2016. Auditory distance perception in humans: a review of cues, development, neuronal bases, and effects of sensory loss. *Attention, Perception, & Psychophysics* 78, 373–395.
- Kong, F., Huang, B., Bradbury, K., Malof, J., 2020. The synthinel-1 dataset: A collection of high resolution synthetic overhead imagery for building segmentation, in: *Proceedings of the IEEE/CVF winter conference on applications of computer vision*, pp. 1814–1823.
- Krizhevsky, A., Sutskever, I., Hinton, G.E., 2012. ImageNet classification with deep convolutional neural networks, in: *Advances in Neural Information Processing Systems (NeurIPS)*, pp. 1097–1105. URL: <https://proceedings.neurips.cc/paper/2012/file/c399862d3b9d6b76c8436e924a68c45b-Paper.pdf>.
- Kunwar, S., 2019a. U-net ensemble for semantic and height estimation using coarse-map initialization, in: *IGARSS 2019-2019 IEEE International Geoscience and Remote Sensing Symposium, IEEE*. pp. 4959–4962.
- Kunwar, S., 2019b. U-net ensemble for semantic and height estimation using coarse-map initialization, in: *IGARSS 2019-2019 IEEE International Geoscience and Remote Sensing Symposium, IEEE*. pp. 4959–4962.
- Lao, J., Wang, C., Zhu, X., Xi, X., Nie, S., Wang, J., Cheng, F., Zhou, G., 2021. Retrieving building height in urban areas using icesat-2 photon-counting lidar data. *International Journal of Applied Earth Observation and Geoinformation* 104, 102596.
- Leotta, M.J., Long, C., Jacquet, B., Zins, M., Lipsa, D., Shan, J., Xu, B., Li, Z., Zhang, X., Chang, S.F., et al., 2019. Urban semantic 3d reconstruction from multiview satellite imagery, in: *Proceedings of the IEEE/CVF Conference on Computer Vision and Pattern Recognition Workshops*, pp. 0–0.
- Li, Q., Mou, L., Hua, Y., Shi, Y., Chen, S., Sun, Y., Zhu, X.X., 2023. 3dcentripetalnet: Building height retrieval from monocular remote sensing imagery. *International Journal of Applied Earth Observation and Geoinformation* 120, 103311.
- Li, S., Zhu, Z., Wang, H., Xu, F., 2019. 3d virtual urban scene reconstruction from a single optical remote sensing image. *IEEE Access* 7, 68305–68315.
- Li, W., Meng, L., Wang, J., He, C., Xia, G.S., Lin, D., 2021. 3d building reconstruction from monocular remote sensing images, in: *Proceedings of the IEEE/CVF International Conference on Computer Vision*, pp. 12548–12557.
- Li, W., Niu, Z., Shang, R., Qin, Y., Wang, L., Chen, H., 2020a. High-resolution mapping of forest canopy height using machine learning by coupling icesat-2 lidar with sentinel-1, sentinel-2 and landsat-8 data. *International Journal of Applied Earth Observation and Geoinformation* 92, 102163.
- Li, W., Yang, H., Hu, Z., Zheng, J., Xia, G.S., He, C., 2024. 3d building reconstruction from monocular remote sensing images with multi-level supervisions. *arXiv preprint arXiv:2404.04823*.
- Li, X., Wang, M., Fang, Y., 2020b. Height estimation from single aerial images using a deep ordinal regression network. *IEEE Geoscience and Remote Sensing Letters* 19, 1–5.
- Liu, J., Gao, J., Ji, S., Zeng, C., Zhang, S., Gong, J., 2023. Deep learning based multi-view stereo matching and 3d scene reconstruction from oblique aerial images. *ISPRS Journal of Photogrammetry and Remote Sensing* 204, 42–60.
- Luthcke, S., Rowlands, D., Williams, T., Sirota, M., 2005. Reduction of icesat systematic geolocation errors and the impact on ice sheet elevation change detection. *Geophysical Research Letters* 32.
- Van der Maaten, L., Hinton, G., 2008. Visualizing data using t-sne. *Journal of machine learning research* 9.
- Magruder, L., Brunt, K., Neumann, T., Klotz, B., Alonzo, M., 2021a. Passive ground-based optical techniques for monitoring the on-orbit icesat-2 altimeter geolocation and footprint diameter. *Earth and Space Science* 8, e2020EA001414.
- Magruder, L., Neuenschwander, A., Klotz, B., 2021b. Digital terrain model elevation corrections using space-based imagery and icesat-2 laser altimetry. *Remote Sensing of Environment* 264, 112621.
- Mahphood, A., Arefi, H., Hosseinimaveh, A., Naeini, A., 2019. Dense multi-view image matching for dsm generation from satellite images. *The International Archives of the Photogrammetry, Remote Sensing and Spatial Information Sciences* 42, 709–715.
- Mao, Y., Chen, K., Zhao, L., Chen, W., Tang, D., Liu, W., Wang, Z., Diao, W., Sun, X., Fu, K., 2023. Elevation estimation-driven building 3d reconstruction from single-view remote sensing imagery. *IEEE Transactions on Geoscience and Remote Sensing*.
- Markus, T., Neumann, T., Martino, A., Abdalati, W., Brunt, K., Csatho, B., Farrell, S., Fricker, H., Gardner, A., Harding, D., et al., 2017. The ice, cloud, and land elevation satellite-2 (icesat-2): science requirements, concept, and implementation. *Remote sensing of environment* 190, 260–273.
- McInnes, L., Healy, J., Melville, J., 2018. Umap: Uniform manifold approximation and projection for dimension reduction. *arXiv preprint arXiv:1802.03426*.
- METI, 2009. Advanced spaceborne thermal emission and reflection radiometer (aster) data. <https://asterweb.jpl.nasa.gov/gdem.asp>. Accessed on 4 March 2025.
- Mou, L., Zhu, X.X., 2018. Im2height: Height estimation from single monocular imagery via fully residual convolutional-deconvolutional network. *arXiv preprint arXiv:1802.10249*.
- NASA, U., 2002. Shuttle radar topography mission (srtm) digital elevation data. <http://usgs.gov/centers/eros/science/usgs-eros-archive-digital-elevation-shuttle-radar-topography-mission-srtm-1>. Accessed on 4 March 2025.
- Neuenschwander, A., Pitts, K., 2019. The atl08 land and vegetation product for the icesat-2 mission. *Remote sensing of environment* 221, 247–259.
- Neumann, T.A., Brenner, A.C., Hancock, D.W., Karbeck, K., Luthcke, S., Robbins, J., Saba, J., Gibbons, A., 2018. Ice, Cloud, and Land

- Elevation Satellite-2 Project Algorithm Theoretical Basis Document for Global Geolocated Photons (ATL03). Technical Report. NASA Goddard Space Flight Center. URL: <https://icesat-2.gsfc.nasa.gov/science/data-products>.
- Neumann, T.A., Martino, A.J., Markus, T., Bae, S., Bock, M.R., Brenner, A.C., Brunt, K.M., Cavanaugh, J., Fernandes, S.T., Hancock, D.W., et al., 2019. The ice, cloud, and land elevation satellite-2 mission: A global geolocated photon product derived from the advanced topographic laser altimeter system. *Remote sensing of environment* 233, 111325.
- Obadic, I., Roscher, R., Oliveira, D.A.B., Zhu, X.X., 2022. Exploring self-attention for crop-type classification explainability. *arXiv preprint arXiv:2210.13167*.
- OLIVER, M.A., WEBSTER, R., 1990. Kriging: a method of interpolation for geographical information systems. *International journal of geographical information systems* 4, 313–332. URL: <https://doi.org/10.1080/02693799008941549>, doi:10.1080/02693799008941549, arXiv:<https://doi.org/10.1080/02693799008941549>.
- Oquab, M., Darcet, T., Moutakanni, T., Vo, H., Szafraniec, M., Khalidov, V., Fernandez, P., Haziza, D., Massa, F., El-Nouby, A., et al., 2023. Dinov2: Learning robust visual features without supervision. *arXiv preprint arXiv:2304.07193*.
- Qi, W., Dubayah, R.O., 2016. Combining tandem-x insar and simulated gedi lidar observations for forest structure mapping. *Remote sensing of Environment* 187, 253–266.
- Ranftl, R., Bochkovskiy, A., Koltun, V., 2021. Vision transformers for dense prediction, in: *Proceedings of the IEEE/CVF international conference on computer vision*, pp. 12179–12188.
- Reyes, M.F., d'Angelo, P., Fraundorfer, F., 2022. Syntcities: A large synthetic remote sensing dataset for disparity estimation. *IEEE Journal of Selected Topics in Applied Earth Observations and Remote Sensing* 15, 10087–10098.
- Reyes, M.F., Xie, Y., Yuan, X., d'Angelo, P., Kurz, F., Cerra, D., Tian, J., 2023. A 2d/3d multimodal data simulation approach with applications on urban semantic segmentation, building extraction and change detection. *ISPRS Journal of Photogrammetry and Remote Sensing* 205, 74–97.
- Roscher, R., Bohn, B., Duarte, M.F., Garcke, J., 2020. Explainable machine learning for scientific insights and discoveries. *Ieee Access* 8, 42200–42216.
- Rupnik, E., Pierrot-Deseilligny, M., Delorme, A., 2018. 3d reconstruction from multi-view vhr-satellite images in micmac. *ISPRS Journal of Photogrammetry and Remote Sensing* 139, 201–211.
- Schmitt, M., Ahmadi, S.A., Xu, Y., Taşkın, G., Verma, U., Sica, F., Hänsch, R., 2023. There are no data like more data: Datasets for deep learning in earth observation. *IEEE Geoscience and Remote Sensing Magazine*.
- Schneider, F.D., Ferraz, A., Hancock, S., Duncanson, L.I., Dubayah, R.O., Pavlick, R.P., Schimel, D.S., 2020. Towards mapping the diversity of canopy structure from space with gedi. *Environmental Research Letters* 15, 115006.
- Selvaraju, R.R., Cogswell, M., Das, A., Vedantam, R., Parikh, D., Batra, D., 2017. Grad-cam: Visual explanations from deep networks via gradient-based localization, in: *Proceedings of the IEEE international conference on computer vision*, pp. 618–626.
- Shendryk, Y., 2022. Fusing gedi with earth observation data for large area aboveground biomass mapping. *International Journal of Applied Earth Observation and Geoinformation* 115, 103108.
- Shepard, D., 1968. A two-dimensional interpolation function for irregularly-spaced data, in: *Proceedings of the 1968 23rd ACM national conference*, pp. 517–524.
- Shermeyer, J., Hossler, T., Van Etten, A., Hogan, D., Lewis, R., Kim, D., 2021. Rareplanes: Synthetic data takes flight, in: *Proceedings of the IEEE/CVF Winter Conference on Applications of Computer Vision*, pp. 207–217.
- Sohn, G., Dowman, I.J., 2004. Extraction of buildings from high resolution satellite data and lidar, in: *XX ISPRS CONGRESS*.
- Song, J., Chen, H., Xuan, W., Xia, J., Yokoya, N., 2024a. Synrs3d: A synthetic dataset for global 3d semantic understanding from monocular remote sensing imagery. *arXiv preprint arXiv:2406.18151*.
- Song, J., Chen, H., Yokoya, N., 2024b. Syntheworld: A large-scale synthetic dataset for land cover mapping and building change detection, in: *Proceedings of the IEEE/CVF Winter Conference on Applications of Computer Vision*, pp. 8287–8296.
- Srivastava, S., Volpi, M., Tuia, D., 2017. Joint height estimation and semantic labeling of monocular aerial images with cnns, in: *2017 IEEE International Geoscience and Remote Sensing Symposium (IGARSS)*, IEEE, pp. 5173–5176.
- Tang, X., Yu, G., Li, X., Taubenböck, H., Hu, G., Zhou, Y., Peng, C., Liu, D., Huang, J., Liu, X., et al., 2025. A flexible framework for built-up height mapping using icesat-2 photons and multisource satellite observations. *Remote Sensing of Environment* 318, 114572.
- Tian, X., Shan, J., 2021. Comprehensive evaluation of the icesat-2 atl08 terrain product. *IEEE Transactions on Geoscience and Remote Sensing* 59, 8195–8209.
- Vaswani, A., 2017. Attention is all you need. *Advances in Neural Information Processing Systems*.
- Wang, C., Zhu, X., Nie, S., Xi, X., Li, D., Zheng, W., Chen, S., 2019. Ground elevation accuracy verification of icesat-2 data: A case study in alaska, usa. *Optics express* 27, 38168–38179.
- Wang, M., Qiu, X., Zhang, Z., Gao, S., 2024. A domain adaptation framework for cross-modality sar 3d reconstruction point clouds segmentation utilizing lidar data. *International Journal of Applied Earth Observation and Geoinformation* 133, 104103.
- Wu, B., Huang, H., Zhao, Y., 2023. Utilizing building offset and shadow to retrieve urban building heights with icesat-2 photons. *Remote Sensing* 15, 3786.
- Xia, J., Chen, H., Broni-Bediako, C., Wei, Y., Song, J., Yokoya, N., 2025. Openearthmap-sar: A benchmark synthetic aperture radar dataset for global high-resolution land cover mapping. *arXiv preprint arXiv:2501.10891*.
- Xiong, Z., Chen, S., Shi, Y., Zhu, X.X., 2024. Self-supervised pre-training with monocular height estimation for semantic segmentation. *IEEE Transactions on Geoscience and Remote Sensing*.
- Xiong, Z., Huang, W., Hu, J., Zhu, X.X., 2023. The benchmark: Transferable representation learning for monocular height estimation. *IEEE Transactions on Geoscience and Remote Sensing*.
- Xu, Y., Huang, B., Luo, X., Bradbury, K., Malof, J.M., 2022. Simpl: Generating synthetic overhead imagery to address custom zero-shot and few-shot detection problems. *IEEE Journal of Selected Topics in Applied Earth Observations and Remote Sensing* 15, 4386–4396.
- You, Z., Tsai, Y.H., Chiu, W.C., Li, G., 2021. Towards interpretable deep networks for monocular depth estimation, in: *Proceedings of the IEEE/CVF International Conference on Computer Vision*, pp. 12879–12888.
- Yu, D., Ji, S., Liu, J., Wei, S., 2021a. Automatic 3d building reconstruction from multi-view aerial images with deep learning. *ISPRS Journal of Photogrammetry and Remote Sensing* 171, 155–170.
- Yu, D., Ji, S., Liu, J., Wei, S., 2021b. Automatic 3d building reconstruction from multi-view aerial images with deep learning. *ISPRS Journal of Photogrammetry and Remote Sensing* 171, 155–170.
- Yu, X., Hyypää, J., Karjalainen, M., Nurminen, K., Karila, K., Vastaranta, M., Kankare, V., Kaartinen, H., Holopainen, M., Honkavaara, E., Kukko, A., Jaakkola, A., Liang, X., Wang, Y., Hyypää, H., Katoh, M., 2015. Comparison of laser and stereo optical, sar and insar point clouds from air- and space-borne sources in the retrieval of forest inventory attributes. *Remote Sensing* 7, 15933–15954. URL: <https://www.mdpi.com/2072-4292/7/12/15809>, doi:10.3390/rs71215809.
- Zeiler, M., 2014. Visualizing and understanding convolutional networks, in: *European conference on computer vision/arXiv*.
- Zhang, G., Chen, W., Xie, H., 2019. Tibetan plateau's lake level and volume changes from nasa's icesat/icesat-2 and landsat missions. *Geophysical Research Letters* 46, 13107–13118.
- Zhang, Z., Wu, J., Zhang, Y., Zhang, Y., Zhang, J., 2003. Multi-view 3d city model generation with image sequences. *INTERNATIONAL ARCHIVES OF PHOTOGRAMMETRY REMOTE SENSING AND SPATIAL INFORMATION SCIENCES* 34, 351–356.

- Zhao, Y., Wu, B., Li, Q., Yang, L., Fan, H., Wu, J., Yu, B., 2023. Combining icesat-2 photons and google earth satellite images for building height extraction. *International Journal of Applied Earth Observation and Geoinformation* 117, 103213.
- Zheng, Z., Zhong, Y., Wang, J., 2019. Pop-net: Encoder-dual decoder for semantic segmentation and single-view height estimation, in: *IGARSS 2019-2019 IEEE International Geoscience and Remote Sensing Symposium*, IEEE. pp. 4963–4966.
- Zou, Z., Shi, T., Li, W., Zhang, Z., Shi, Z., 2020. Do game data generalize well for remote sensing image segmentation? *Remote Sensing* 12, 275.